

P
2mip

SQT

August 1973

LMSC-D352320

UNSTEADY AERODYNAMIC ANALYSIS OF SPACE SHUTTLE VEHICLES

Part IV: EFFECT OF CONTROL DEFLECTIONS ON ORBITER UNSTEADY AERODYNAMICS

Final Technical Report



Prepared by
J. Peter Reding
Research Specialist Aero-Thermodynamics
Lars E. Ericsson
Consulting Engineer, Engineering Technology

Prepared Under Contract NAS 8-28130
for
National Aeronautics and Space Administration

NASA-CR-120125) UNSTEADY AERODYNAMIC
ANALYSIS OF SPACE SHUTTLE VEHICLES.
PART 4: EFFECT OF CONTROL DEFLECTIONS
ON ORBITER UNSTEADY (Lockheed Missiles
and Space Co.) 66 p HC \$5.50 CSCI 22B

G3/31
26373
Unclas
N74-15532

Lockheed MISSILES & SPACE COMPANY, INC.
SUNNYVALE, CALIFORNIA

UNSTEADY AERODYNAMIC ANALYSIS
OF SPACE SHUTTLE VEHICLES

Part IV: EFFECT OF CONTROL
DEFLECTIONS ON ORBITER
UNSTEADY AERODYNAMICS

by

J. Peter Reding and Lars E. Ericsson

August 1973

Prepared Under Contract NAS 8-28130

for

National Aeronautics and Space Administration

Lockheed Missiles & Space Company, Inc.
A Subsidiary of Lockheed Aircraft Corporation
Sunnyvale, California

PRECEDING PAGE BLANK NOT FILMED

ABSTRACT

The unsteady aerodynamics of the 040A orbiter have been explored experimentally. The results substantiate earlier predictions of the unsteady flow boundaries for a 60° swept delta wing at zero yaw and with no controls deflected. The test revealed a previously unknown region of discontinuous yaw characteristics at transonic speeds. Oilflow results indicate that this is the result of a coupling between wing and fuselage flows via the separated region forward of the deflected elevon. In fact, the large leeward elevon deflections are shown to produce a multitude of nonlinear stability effects which sometimes involve hysteresis.

Predictions of the unsteady flow boundaries are made for the current orbiter. They should carry a good degree of confidence due to the present substantiation of previous predictions for the 040A. It is proposed that the present experiments be extended to the current configuration to define control-induced effects. Every effort should be made to account for Reynolds number, roughness, and possible hot-wall effects on any future experiments.

PRECEDING PAGE BLANK NOT FILMED

CONTENTS

Section		Page
	ABSTRACT	iii
	ILLUSTRATIONS	vii
1	INTRODUCTION	1-1
2	WIND TUNNEL TEST	2-1
3	DATA ANALYSIS	3-1
	3.1 Subsonic Pitch Results	3-1
	3.2 Supersonic Pitch Results	3-7
	3.3 Yaw Stability Results	3-9
	3.4 Current Orbiter Unsteady Flow Boundaries	3-11
4	CONCLUSIONS	4-1
5	RECOMMENDATIONS FOR FUTURE STUDY	5-1
6	REFERENCES	6-1
Appendix		
A	NOMENCLATURE	A-1

~~PRECEDING~~ PRECEDING PAGE BLANK NOT FILMED

ILLUSTRATIONS

Figure		Page
1.	Comparison of Predicted and Measured Unsteady Flow Boundaries for the 040A Orbiter	1-2
2.	Orbiter Configurations	1-3
3.	040A Orbiter Pitch Stability at $M = 0.9$	3-14
4.	040A Orbiter Surface Flow Patterns, $M = 0.9$, $\delta_L = -40^\circ$, $\delta_R = 0$	3-16
5.	040A Orbiter Elevon Control Effectiveness	3-21
6.	040A Orbiter Pitch Stability at $M = 0.6$	3-22
7.	040A Orbiter Pitch Stability at $M = 1.46$	3-24
8.	040A Orbiter Elevon Control Characteristics at $M = 0.9$	3-26
9.	040A Orbiter Surface Flow Patterns in α Hysteresis Region; $M = 1.46$, $\alpha = 22^\circ$, $\delta_L = -40^\circ$, $\delta_R = 0$	3-27
10.	040A Orbiter Pitch Stability at $M = 2.99$	3-30
11.	040A Orbiter Surface Flow Patterns; $M = 2.99$, $\delta_L = -40^\circ$, $\delta_R = 0$	3-32
12.	040A Orbiter Yaw Stability; $M = 0.9$, $\alpha = 11^\circ$, $\delta_L = -40^\circ$, $\delta_R = 0$	3-35
13.	040A Orbiter Yaw Stability; $M = 0.6$, $\alpha = 10.4^\circ$, $\delta_L = -40^\circ$, $\delta_R = 0$	3-36
14.	040A Orbiter Yaw Stability, $M = 1.46$, $\alpha = 11.4^\circ$, $\delta_L = -40^\circ$, $\delta_R = 0$	3-37
15.	040A Orbiter Flow Field Due to Yaw at $M = 0.9$, $\alpha = 10^\circ$, $\delta_L = -40^\circ$, $\delta_R = 0$	3-38
16.	040A Orbiter Surface Flow Patterns Due to Yaw at $M = 1.46$, $\alpha = 11^\circ$, $\delta_L = -40^\circ$, $\delta_R = 0$	3-40
17.	040A Orbiter Yaw Stability, $M = 1.46$, $\alpha = 22.4^\circ$, $\delta_L = -40^\circ$, $\delta_R = 0$	3-42

ILLUSTRATIONS (Continued)

Figure		Page
18.	Estimated Unsteady Flow Boundaries for Current Orbiter	3-43
19.	Evidence of Strake Vortex on Current Orbiter, $M = 4.96$, $\alpha = 20^\circ$, $\beta = 0$	3-44
20.	Vortex Burst Location and Hysteresis for Strake Alone at Subsonic Speeds	3-45

TABLE

Table		
I	Summary of Test Conditions	5-3

Section 1 INTRODUCTION

A previous study of the unsteady aerodynamics of a typical phase B orbiter revealed that the vehicle dynamics could be dominated by a number of unsteady flow phenomena (Ref. 1). Essentially three unsteady wing flows were identified which could adversely affect stability. They are:

1. Leeward shock-induced separation
2. Sudden leading edge stall
3. Leading edge vortex burst.

Furthermore, large leeward elevon deflections were found to alter dramatically the flow field on the leeward side of the wing. Thus, it appeared quite possible that asymmetric wing flow patterns could occur for a combined pitch-roll command that could result in snap roll. Likewise, control hysteresis might be expected due to the control-induced effects on the wing flow patterns.

A wind tunnel test has been conducted on the 040A orbiter to investigate the effects of flow separation on the orbiter stability and control. Fortunately, the 040A wing is quite similar to that of the phase B orbiter used in the earlier study (both are basically 60° delta wings). Thus, the 040A data could be used to test the veracity of the flow boundaries predicted in the earlier study (Ref. 1). The agreement is quite good (Fig. 1). Unfortunately, the orbiter configuration has changed significantly over the past year, and the new configuration is quite different from the 040A (Fig. 2). However, the changes are not so drastic as to completely invalidate what was learned from the earlier work. In the following discussion, the 040A data are analyzed and the knowledge gained from the analysis is used to identify areas of concern relative to the unsteady aerodynamics of the current configuration.

1-2

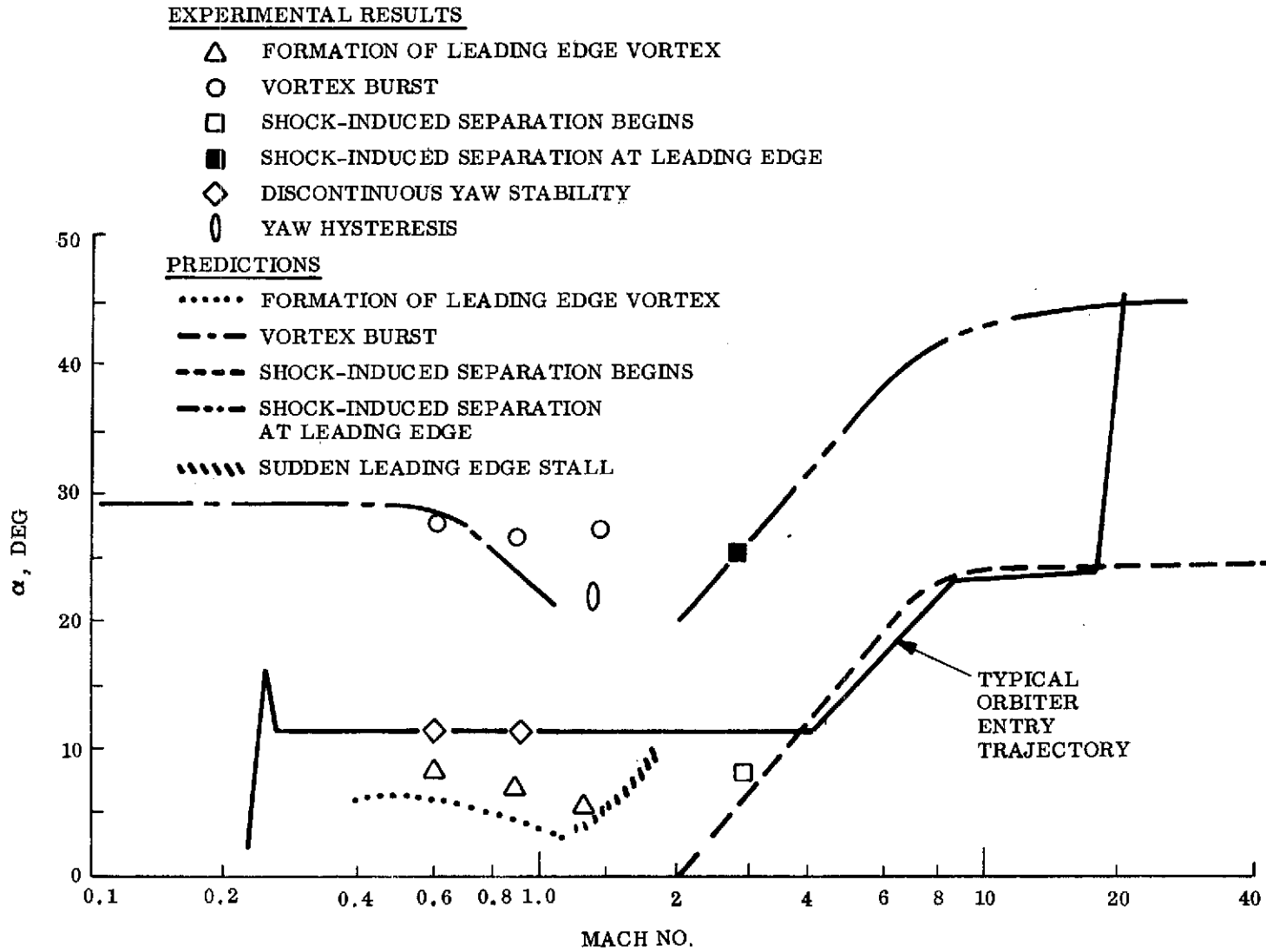
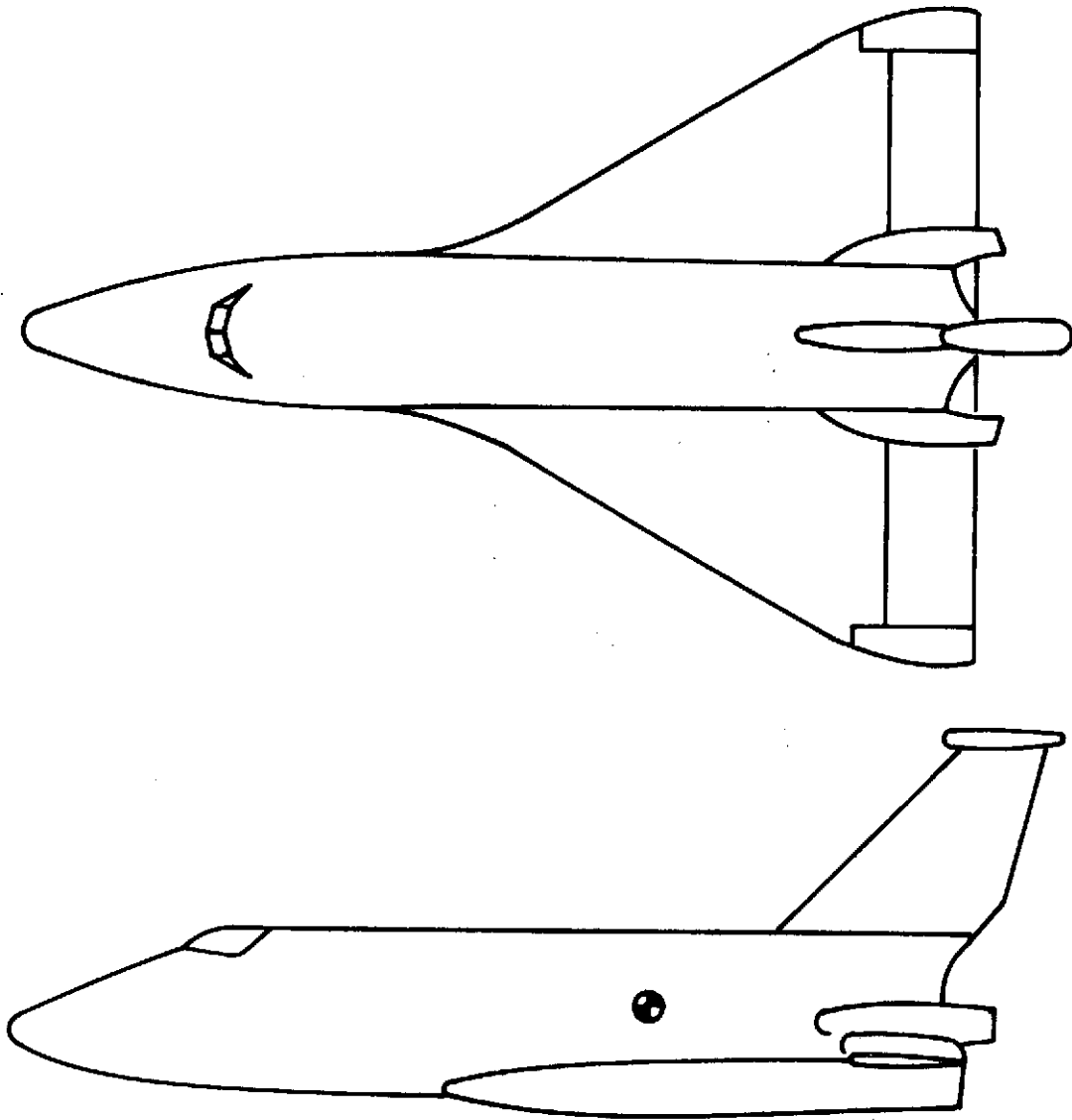
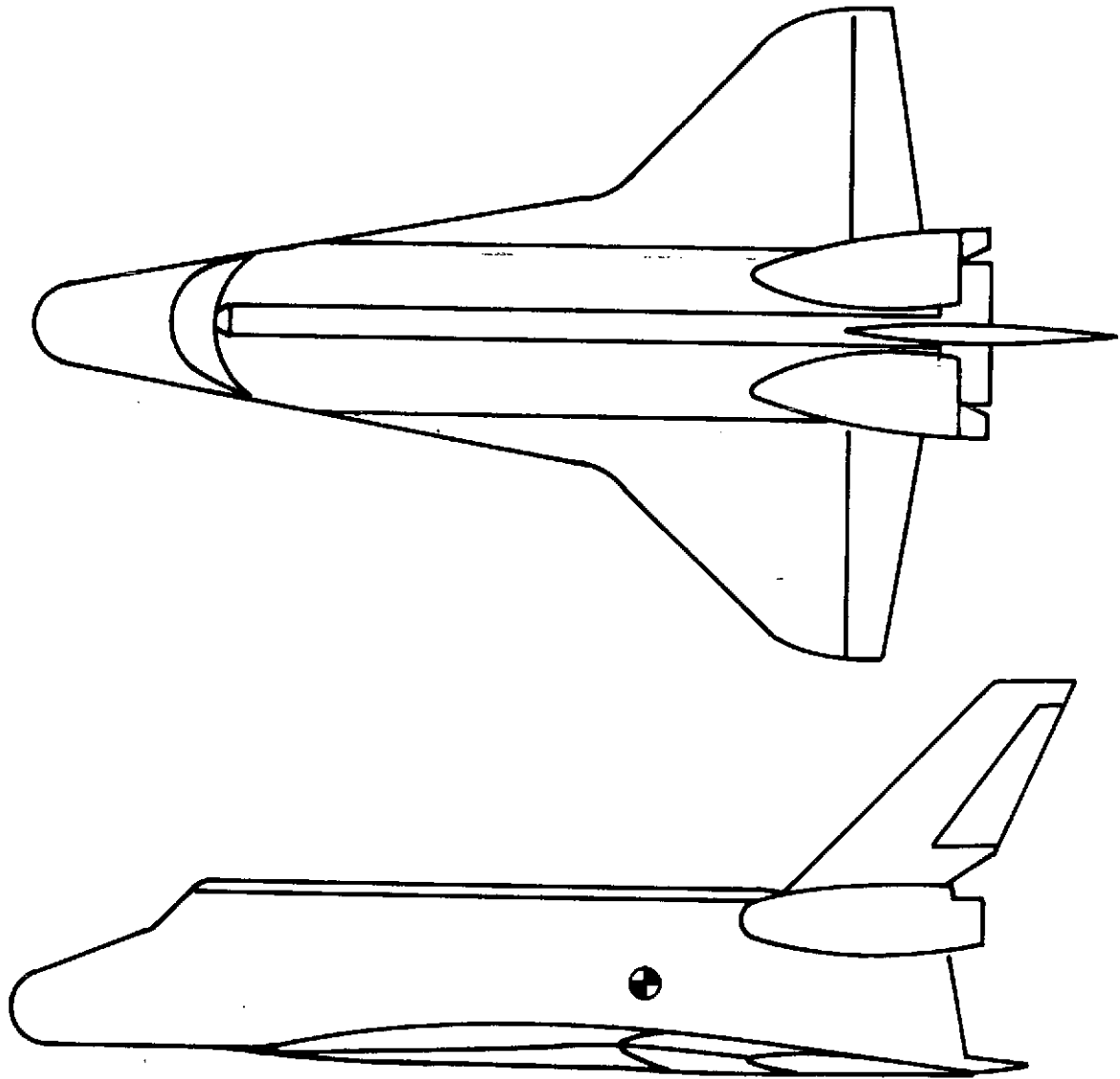


Figure 1. Comparison of Predicted and Measured Unsteady Flow Boundaries for the 040A Orbiter



a. 040A ORBITER

Figure 2. Orbiter Configurations (Sheet 1 of 2)



b. CURRENT ORBITER

Figure 2. Orbiter Configurations (Sheet 2 of 2)

Section 2
WIND TUNNEL TEST

A 0.6% scale model of the MSC 040A orbiter (Fig. 2) was tested in the MSFC 14-inch Trisonic Wind Tunnel. A complete summary of the facility operating conditions may be found in Ref. 2. The test objective was to gain insight into the flow field phenomena associated with the large leeward deflections of the trailing edge elevons. Only the left elevon was deflected, the deflections (δ_L) being -5° , -20° , and -40° . In this manner, the roll, yaw, and side force data could be used most effectively to describe the control-induced flow phenomena. In addition to six-component force and moment data, a large number of oilflow photographs were obtained.

Section 3 DATA ANALYSIS

The test results for the 040A orbiter show that the critical flow boundaries can be predicted with confidence (Fig. 1). The boundaries of the region of shock-induced separation agree quite well with predictions. Vortex burst is also well predicted. Unfortunately, experimental results were not obtained in the region of sudden leading edge stall to test the predictions made from the straight wing data of Ref. 3. However, as the leading edge stall boundary of Ref. 3 comes close to predicting the formation of the leading edge vortex, one would expect that the sudden stall boundaries would also be predicted rather well. The boundaries are for $\beta = 0$ and $\delta = 0$ and were defined from evidence of alterations in the flow conditions on the right wing (where $\delta_R = 0$ in the present test). With the exception of this evidence, which is described more fully later in the following discussion, the analysis concentrates on the control-induced effects (on the left wing).

3.1 Subsonic Pitch Results

It is evident from Fig. 3 that the orbiter stability and control characteristics are highly nonlinear about all three body axes. The correlation between rolling moment, yawing moment, and side force nonlinearities is indicative of the strong coupling that results because the elevon affects the flow over both the wing and the fuselage. This is illustrated by the oilflow photographs in Fig. 4 and the accompanying interpretive flow sketches.

Essentially three distinctly different wing flows occur at subsonic speeds. Each has its own unique effects on the stability. They are:

1. Attached leading edge flow
2. Stable leading edge vortex
3. Breakdown or burst of the leading edge vortex.

The lateral and directional stability coefficients are most sensitive to changes in wing flow patterns (Fig. 3a). For example, for the large leeward elevon deflection ($\delta_L = -40^\circ$), a large flow separation is induced forward of the elevon on both the fuselage and the wing. At low angle of attack (e.g., $\alpha \leq 8^\circ$, Fig. 3a), the leading edge flow is attached and the elevon-induced separation is ventilated outboard at the wing tip and upward over the aft fuselage (see Fig. 4a). The flow separation induces upwash and sidewash over the aft fuselage, including the vertical tail. This sidewash adds to the effect of the pressure rise in the separated flow region. Together they produce a positive side force and a negative yawing moment. Unfortunately, oilflow photographs were obtained only for the highest elevon deflection ($\delta_L = -40^\circ$). In order to understand how the separation progresses with increasing control deflection, one has to study the control effectiveness data shown in Fig. 5. Along with the $M = 0.9$ data from Fig. 3, $M = 0.6$ and $M = 1.46$ data from Figs. 6 and 7, respectively, are included.* The side force and yawing moment data indicate that the separated region at the wing-fuselage juncture grows with increasing elevon deflection, and the separated region is largest at $M = 0.9$, as one might expect. Oilflow results also verify that the separation is largest at $M = 0.9$.

The pitching and rolling moment data in Fig. 5 show nonlinear trends opposite those of the side force and yawing moment data. A complete loss in pitch and roll control effectiveness occurs for $-\delta_L > 20^\circ$, whereas the C_Y and C_n data show increased control effectiveness (Fig. 5). The oilflow photographs in Fig. 4 show that reattachment occurs at approximately the midchord of the elevon. Thus, the loss of roll control does not result from the elevon being completely engulfed by the flow separation. With no oilflow results available for intermediate elevon deflections between $\delta_L = 0$ and $\delta_L = -40^\circ$ one is forced to speculate about the causes of the nonlinear control effects.

*Only the pitching moment results have a $\delta_L = 0$ reference. These data are from Ref. 4 for an 040A orbiter with a more bulbous canopy. For the other coefficients, it is possible that the data may contain zero offsets.

The pitch results for $\delta_L = -40^\circ$ indicate that the flow at the wing-fuselage juncture is extremely sensitive to angle of attack (Figs. 4a through 4e). It is logical to assume that the corner flow is also very sensitive to δ_L variations. As δ_L is changed from -5° to -20° , flow separation occurs in the channel formed by the wing, fuselage, and orbital maneuvering system (OMS) pod. Because the control effectiveness remains roughly linear, the increase in the separation extent forward of the elevon and the locally higher pressures there are evidently balanced by the growth of the separated region on the elevon and the incrementally lower local pressures there. For relatively small elevon deflections ($-5^\circ > \delta_L > -20^\circ$), the OMS pod restricts but does not entirely preclude venting of the separated region at the wing body juncture. However, because of the restricting effect of the OMS pod, most of the venting must occur at the elevon edge near the wing tip. This results in a relatively large region of separation forward of the elevon. Somewhere between $\delta_L = -20^\circ$ and $\delta_L = -40^\circ$ the channel between the fuselage, wing, and OMS pod is effectively closed off. The corner separation, therefore, suddenly expands and spills over the forward end of the pod, causing a sidewash on the aft fuselage and vertical fin (see insert sketches in Fig. 5). The sidewash is very evident in the oilflow on the top of the model (Fig. 4a). At subsonic speeds, the air forward of the separation "feels" the presence of the separation; and the sidewash, upwash, and accompanying pressure rise on the left side of the fuselage grows more or less linearly. Thus, $C_Y(\delta_L)$ and $C_n(\delta_L)$ are nearly linear for $M < 1.0$ (Fig. 5). At supersonic speeds, there is no upstream sensing, and $C_Y(\delta_L)$ and $C_n(\delta_L)$ are highly nonlinear as the separation suddenly involves the fuselage above the OMS pod and generates a sidewash on the vertical fin.

The sidewash on the fin causes a positive rolling moment increment. The separation on the wing also skews, because venting of the separation bubble is no longer restricted by the OMS pod. Thus, the flow in the recirculation region no longer needs to be funneled spanwise to the outboard tip of the elevon but can vent at the wing-fuselage juncture. The separation, therefore, tends to contract outboard, which also contributes to the positive rolling moment increment. Both effects are opposite to the intended effect of the elevon deflection, and the control effectiveness in roll is therefore decreased. The increased venting at the wing-fuselage juncture due to the

"popping" separation tends to reduce the rate of growth of the separated region. This reduction, coupled with any aft fuselage lift due to the induced upwash, produces a stabilizing C_m effect; i. e., the control effectiveness in pitch is also reduced.

There is every reason to suspect that the "popping" separation phenomenon discussed above will be associated with hysteresis effects, and it is also possible that outright elevon reversal will occur somewhere between $\delta_L = -20^\circ$ and $\delta_L = -40^\circ$. Even without these effects, the ever-present flow field time lag (Ref. 1) can cause the separated flow to have highly undesirable effects on the vehicle dynamics. Thus, it is desirable to eliminate the "popping" separation. Of the several means available, moving the pod away from the elevon is probably the simplest. However, the beneficial effects of moving the pod could be cancelled by an increase in the pod size. Thus, it is not readily apparent if the new orbiter configuration (which incorporates both changes) is superior or not to the 040A in this respect. Increasing the gap between the inboard edge of the elevon and the fuselage is another means of avoiding the "popping" separation by increasing the venting at the wing-fuselage juncture. It may also be possible to program the deflection of the split elevon for the new configuration such that the deflection of the inboard elevon panel is kept below 20° or whatever the critical value is for this particular configuration.

At higher angles of attack, vortex burst begins to dominate (see Fig. 4c). For a 60° delta wing with a sharp leading edge, burst occurs at the trailing edge at $\alpha \approx 15^\circ$ and moves to the apex at $\alpha \approx 28^\circ$ (Ref. 1). The deflected elevon acts as Hummel's downstream obstacle (Ref. 5) if it is directly in the vortex path. In the case of the 040A, the elevon is slightly to the side of the vortex path; and its burst-producing capability is greatly moderated. The data in Fig. 3a indicate that burst starts on the left wing at $\alpha \approx 16^\circ$ for $\delta_L = -5^\circ$.* As the burst progresses upstream toward the apex, the loss of core suction on the left wing with associated loss of lift causes a negative C_L . This is accompanied by an increase in the positive C_Y and a more negative C_n due to the burst-induced positive pressure increment on the fuselage side.

*The delay of burst relative to the sharp wing is the result of the round leading edge.

At $\alpha > 28^\circ$, the vortex burst approaches the apex on the right wing and C_ℓ , C_Y , and C_n tend toward zero as the pressures are equalized on both wings.

When the elevon deflection is altered to $\delta_L = -20^\circ$ and $\delta_L = -40^\circ$, the simple situation outlined above is complicated by elevon-induced separated flow effects. For $\delta_L = -20^\circ$ and $\delta_L = -40^\circ$, burst seems to start on the left wing only slightly sooner than when $\delta_L = -5^\circ$ (Fig. 3a). This effect is the result of the flow separation limiting the extent and level of the pressure rise upstream of the elevon. Qualitatively, the burst effects for $\delta_L = -20^\circ$ and $\delta_L = -40^\circ$ are similar to the effect at $\delta_L = -5^\circ$, except that the burst-induced stability increments are applied to a C_Y that is decreasing with α and to a C_ℓ and C_n that are increasing with α rather than to constant values as was the case for $\delta_L = -5^\circ$. The α slopes (Figs. 3, 6, and 7) are the result of the leading edge vortex affecting the separation extent. The leading edge vortex is essentially a leading edge separation that is vented by a strong spanwise flow component, thus creating a leading edge vortex. The vortex acts as a pre-separation which strengthens the downstream boundary layer (Ref. 6). The leading edge boundary layer is trapped in the separated region and bled off via the leading edge vortex. A new, stronger boundary layer, formed downstream of the vortex reattachment, is harder to separate and thus causes a contraction of the elevon-induced separation. As the vortex grows with α , the boundary layer is strengthened further and the separation continues to shrink. This is illustrated well by the oilflow photographs (compare Figs. 4a and 4b). As a consequence, the control-induced separation is decreased, resulting in the observed decrease of the elevon-induced control increments (compare $\alpha = 8^\circ$ with $\alpha = 15^\circ$ in Figs 3 and 8).

Vortex burst accelerates the collapse of the separated region, as is evident in the oilflow photographs for $\alpha \geq 20^\circ$ (compare Figs. 4c, 4d, and 4e). At $\alpha = 30^\circ$, the separation has vanished except for a small bubble in the corner of the wing-fuselage juncture under the OMS pod. Thus, the positive side force and the negative yawing and rolling moment increments generated by the large elevon-induced separation are lost. The small residual separation at the wing-fuselage juncture does, however, supply a strong spanwise pressure gradient. Thus, the flow on the left wing forward of the elevon has a strong spanwise component (see top oilflow photographs in Figs. 4d

and 4e). This forces the burst vortex further outboard on the left wing. As a result, the center of pressure of the left wing is further outboard than that of the right wing, causing a residual negative rolling moment when burst dominates both wings ($\alpha \geq 28^\circ$ in Fig. 3a). The deflected left elevon also limits the wing and associated area on the fuselage side that can be affected by the vortex-burst-induced pressure rise. As a consequence, the right wing-fuselage juncture dominates the side force for high angles of attack, $\alpha \geq 28^\circ$ (i. e., C_Y is negative). The local separation under the OMS pod generates a concentrated positive C_Y component that, because of its larger lever arm, cancels the effect on C_n of the larger right wing C_Y component; thus C_n is approximately zero for $\alpha \geq 28^\circ$.

The leeside fuselage flow patterns exhibit significant changes throughout the angle-of-attack range (Fig. 4). For $\alpha \geq 10^\circ$, a small region of separation occurs on top of the canopy which is vented by a small pair of counter-rotating vortices (see Fig. 4a). Further downstream, the upper fuselage flow is dominated by the elevon-induced side-wash, as previously discussed. At $\alpha \approx 10^\circ$, strong leeside vortices begin to develop on the upper fuselage, as evidenced by the feathering reattachment flow patterns on the fuselage top (Fig. 4b). These vortices are separate from and rotate opposite to the vortices venting the canopy separation. They cause a flattening of the pitching moment curves in the vicinity of 10° due to the induced lift on the forward fuselage* (Fig. 3b). The pitching moment steepens again at higher α , owing to the stabilizing effect of the wing leading edge vortices.

It is interesting to note that at $M = 0.9$ a terminal shock seems to be present on the fuselage sides at $\alpha \geq 10^\circ$ (see Fig. 4). The shock front angles downward and aft from the canopy to the wing apex. It appears as a slight discontinuity in the oil streaks (for $\alpha = 10^\circ$, but not for $\alpha = 6^\circ$) and is depicted by a dashed line in the flow sketch. The shock increases in strength as angle of attack increases until at $\alpha = 20^\circ$ it causes local flow separation which determines the starting location of the leeside vortices (Fig. 4c). A local separation bubble apparently develops on the fuselage

*The blunter cabin on the model used to measure the $\delta_L = 0$ results, Ref. 4, accounts for the earlier occurrence of the flattening.

corner just forward of the wing due to the small corner radius there. This "preseparation" (Ref. 6) strengthens the fuselage boundary layer locally and causes a discontinuity in the shock-induced separation front on the fuselage side. With the exception of this shock-induced separation, the $M = 0.9$ results appear to be typical for high subsonic speeds, judging by their similarity to the $M = 0.6$ data (compare Figs. 3 and 6).

3.2 Supersonic Pitch Results

The effects of angle of attack on stability and control characteristics at $M = 1.46$ are in many respects similar to the effects at $M = 0.9$ (compare Figs. 3, 5, and 7). The characteristics are in both cases dominated by similar wing flow patterns. The main difference is to be found in the fuselage flow patterns. At $M = 1.46$, the shock that slants downward and aft from the canopy on the fuselage sides is highly oblique and extends nearly to the OMS pod (Figs. 9 and 16). Thus, free-body vortices in the usual sense are never generated, which explains the lack of flattening in the C_m curves at $\alpha = 10^\circ$ (compare Figs. 3b and 7b).

At $\alpha = 22^\circ$, the leading edge vortex begins to burst near the left wing tip. This causes a sudden collapse of the elevon-induced separation as the leading edge vortex, suddenly expanded by burst, engulfs the elevon (compare Figs. 9a and 9b). This results in discontinuities with associated α -hysteresis for the moment coefficients (C_ℓ , C_n , and C_m) that are the most sensitive to elevon effects (Fig. 7). Hysteresis is not unusual when vortex burst is involved (Ref. 7). The addition of an outboard spoiler seems to have eliminated some of the effect of the leading edge vortex, both before and after burst, judging by the lower magnitudes of C_ℓ , C_m , and C_n (see Fig. 7 and 9c). However, the discontinuity and hysteresis are only reduced, not completely eliminated. Extending the spoiler further inboard should eliminate the hysteresis.

At $M = 2.99$, the pitch results differ drastically from those previously discussed (compare Fig. 10 with Figs. 3, 6, and 7). These data are similar to results identified as being typically hypersonic in Ref. 1. In fact, the flow field is quite similar to the hypersonic wing flow observed by Cross on a pure delta wing (Ref. 8) and by Seegmiller on an earlier shuttle configuration (Ref. 9). At low angles of attack, the flow on the leeward side of the delta wing is attached and the wing flow is turned parallel to the fuselage by a weak oblique shock (Fig. 11a). The α -trends for $\alpha < 7^\circ$ are very different from those shown earlier for lower Mach numbers. This could mean simply that at $M = 2.99$, the separation-delaying effect of the α -induced increase of the local Mach number dominates the separation-promoting effect of the α -induced adverse pressure gradient, which is small for the supersonic leading edge condition that occurs at low α . The opposite is true for $M = 1.46$. If $M_{\text{local}} > 3.25$, no turbulent boundary layer separation would occur at $\alpha = 0$ for $\delta = -20^\circ$ (Ref. 10).

At $\alpha = 7^\circ$, the wing bow shock detaches, giving a subsonic leading edge. The flow normal to the leading edge expands over the leeside of the wing, reattaining supersonic speeds. The flow is turned parallel to the fuselage via a strong shock that separates the boundary layer. Because of the spanwise flow component, the separation bubble is vented at the tip and resembles a leading edge vortex (Fig. 11b). The shock-induced separation occurs on both wings simultaneously. The resulting pressure increase on the leeward side causes an unstable pitching moment increment which is responsible for the flattening of the C_m -versus- α curve at $\alpha \approx 10^\circ$ (Fig. 10b). Elevon deflection promotes separation, causing a larger destabilizing C_m increment. The upstream shock-induced separation furnishes a pre-separation effect for the elevon-induced separation that occurs at large negative δ_L . This results in the usual strengthening of the downstream boundary layer and causes a contraction of the elevon-induced separation (compare Figs. 11a and 11b). In this manner, C_Y and C_n continue their trend toward zero for high angles of attack. It should be pointed out, however, that the C_Y , C_n , and C_ℓ scales are exaggerated (by a factor of 5) relative to the $M = 0.6$, $M = 0.9$, and $M = 1.46$ results (compare Fig. 10 with Figs. 3, 6, and 9). Thus, the C_Y and C_n residuals for $\alpha \geq 20^\circ$ should not be taken too seriously, particularly in view of the discontinuity in C_Y at $\alpha = 20^\circ$ due to the change in sting offset angle.

The shock-induced separation moves forward with angle of attack until it is locked to the leading edge. This happens at $\alpha = 25^\circ$ for $\delta_L = 0$ (see Fig. 1). When the forward movement of the shock-induced separation is arrested at the leading edge, the negative force generation due to an enlarging region of positive pressure is stopped. This causes the $C_m(\alpha)$ curve to turn down again (Fig. 10b). The oilflow photographs in Fig. 11c show that the left wing has leading edge stall at $\alpha \geq 24^\circ$ when $\delta_L = -40^\circ$. The pitching moment shows the typically supersonic, stable, nonlinearity with angle of attack which results from the dominance of the positive windward side pressures on the wing lift. This is also seen in the $C_N(\alpha)$ curve, which does not experience the decrease in slope at high α that was observed at $M = 1.46$. This effect also accounts for the increase of C_L with α when C_Y and C_n are effectively negligible.

3.3 Yaw Stability Results

The pitch stability characteristics discussed above were not altogether unexpected. Many of the flow features involved have either been observed on other orbiter configurations or have been postulated based on evidence from other delta-winged configurations (Ref. 1). It is, of course, to be expected that the yaw characteristics might also be nonlinear. However, the discontinuous characteristics shown in Fig. 12 were still somewhat of a surprise. The stability characteristics are discontinuous about all three body axes at $\alpha = 11^\circ$, which is very close to the proposed transonic trim angle of 10° . (The same yaw discontinuity will undoubtedly occur at $\alpha = 10^\circ$.) Similar highly nonlinear yaw derivatives were also observed at $M = 0.6$ (Fig. 13); but at $M = 1.46$, the discontinuities had vanished (Fig. 14). These highly nonlinear or discontinuous yaw stability characteristics could have a dominating influence on the orbiter dynamics for combined pitch and roll control deflections.

All the data shown in Figs. 12 through 14 were obtained with a -40° control deflection on the left elevon ($\delta_L = -40^\circ$); and the discontinuous yaw characteristics are, of course, caused by the same "popping" separation phenomenon that was discussed earlier in connection with the loss of control effectiveness (Fig. 5).

However, in this case, it is the strength of the boundary layer on the fuselage sides that drives the "popping." At $\beta > 0$, the left side of the fuselage is on the leeward side of the yaw plane flow. The resulting increase of the adverse pressure gradient, along with the thickening of the boundary layer due to crossflow effects at the nose, produces an enlargement of the region of elevon-induced separation at the left wing-fuselage juncture. The separation, therefore, "pops" out from under the OMS pod (Fig. 15a). The sudden expansion of the separation in the corner causes a negative incremental C_N (as before) which dominates $C_m(\beta)$, producing a positive moment increment (Fig. 12). The skewing of the separation line forward of the elevon (greater inboard than outboard) from a more or less constant separation extent causes a positive C_ℓ increment. The displaced left fuselage vortex (compare Fig. 15a and 15b) interacts with the vertical fin, causing a negative C_Y increment because the vortex core with its suction is closer to the left side of the fin. The negative C_Y on the tail gives a negative C_ℓ , which limits but does not overcome the positive C_ℓ increment caused by the skewed elevon-induced separation. It does, however, cancel the positive C_Y increment produced on the aft fuselage; thus, C_Y exhibits no nonlinearity. This body-vortex-induced tail load, because of its aft location, dominates C_n and accounts for the positive C_n discontinuity (Fig. 12). Of course, for $\beta < 0$, the boundary layer on the left side of the fuselage becomes the strongest; and the separation "pops" back under the OMS pod (Fig. 15b), causing a reversal of these effects. Similar effects occur at $M = 0.6$ (Fig. 13).

At $M = 1.46$, the flow field appears similar (Fig. 16). That is, the extent of the separated region seems to exhibit similar changes in geometry, although the stability data do not show drastic results (compare Fig. 14 with Figs. 12 and 13). This is interesting because the $M = 1.46$ oilflow photographs for β variations (Fig. 16) were used along with those for $M = 0.9$ and $\beta = 0$ (Fig. 4) to infer the yaw flow field at $M = 0.9$ just discussed (Fig. 15). The fundamental difference between the flow fields at $\alpha = 11^\circ$ for $M = 0.9$ and $M = 1.46$ involves the fuselage vortices. At $M = 1.46$, the usual leeward fuselage vortices do not occur on the top of the fuselage. The shock front stretches downward aft of the canopy and almost reaches the OMS pod (Fig. 16). This causes a separated region that is vented via vortices restricted to the fuselage sides, which cannot interact with the vertical tail as readily. The shock-induced

separation also tends to stabilize the boundary layer on the fuselage sides via the preseparation effect. The result is an almost complete absence of any nonlinearity at $M = 1.46$. This demonstrates that the effect of the fuselage vortices on the subsonic yaw characteristics ($M = 0.6$ and $M = 0.9$) was substantial.

Some significant hysteresis loops occur at $M = 1.46$ and $\alpha = 22.4^\circ$ (Fig. 17). This hysteresis is evidently associated with the same vortex burst effects that caused the α hysteresis (Fig. 7). The vortex burst that occurs on the right wing at $\alpha = 22.4^\circ$, $\beta = 0^\circ$ diminishes gradually for $\beta \geq 1^\circ$ as the sweep of the right wing is effectively decreased. The opposite occurs on the left wing; thus, the C_N and C_m curves are relatively flat. There is evidently some delay in reestablishing burst as β is decreased from positive values. This causes the observed hysteresis in C_m and C_ℓ (the most sensitive stability coefficients).

3.4 Current Orbiter Unsteady Flow Boundaries

The current test results not only verify the unsteady flow boundaries of Ref. 1, but they reveal previously unknown regions of discontinuous pitch and yaw characteristics, one of which is coincident with the subsonic-transonic cruise angle of attack. The success in predicting the unsteady flow boundaries for the 040A configuration lends confidence to the predictions for the current orbiter (Fig. 18). The current orbiter successfully avoids the region of shock-induced separation over nearly the entire trajectory except for a relatively quick traverse between $M = 2.4$ and $M = 1.5$. However, it takes the orbiter about 90 seconds for even this quick traverse, allowing sufficient time for roll oscillations to grow to a significant magnitude if undamping occurs, as appears possible (Ref. 1). Practically, it is possible that shock-induced separation could occur at a lower angle of attack due to leading edge bluntness and fuselage back-pressure effects (Ref. 11). However, for the current α - M trajectory, the duration of shock-induced separation would not be significantly affected.

The orbiter flies well above the region of shock-induced separation on the strake. Although the upper boundary of this region cannot now be predicted, Cross (Ref. 9)

has shown that for a 75° swept pure delta wing at $M = 11$, the shock becomes locked to the leading edge at $\alpha = 21^\circ$. For the 80° leading edge sweep of the strake, this occurs at lower α (Ref. 1). Thus, it is very unlikely that the strake will experience shock-induced separation. In fact, one can expect that a leading edge vortex will occur on the strake over the entire Mach number range.

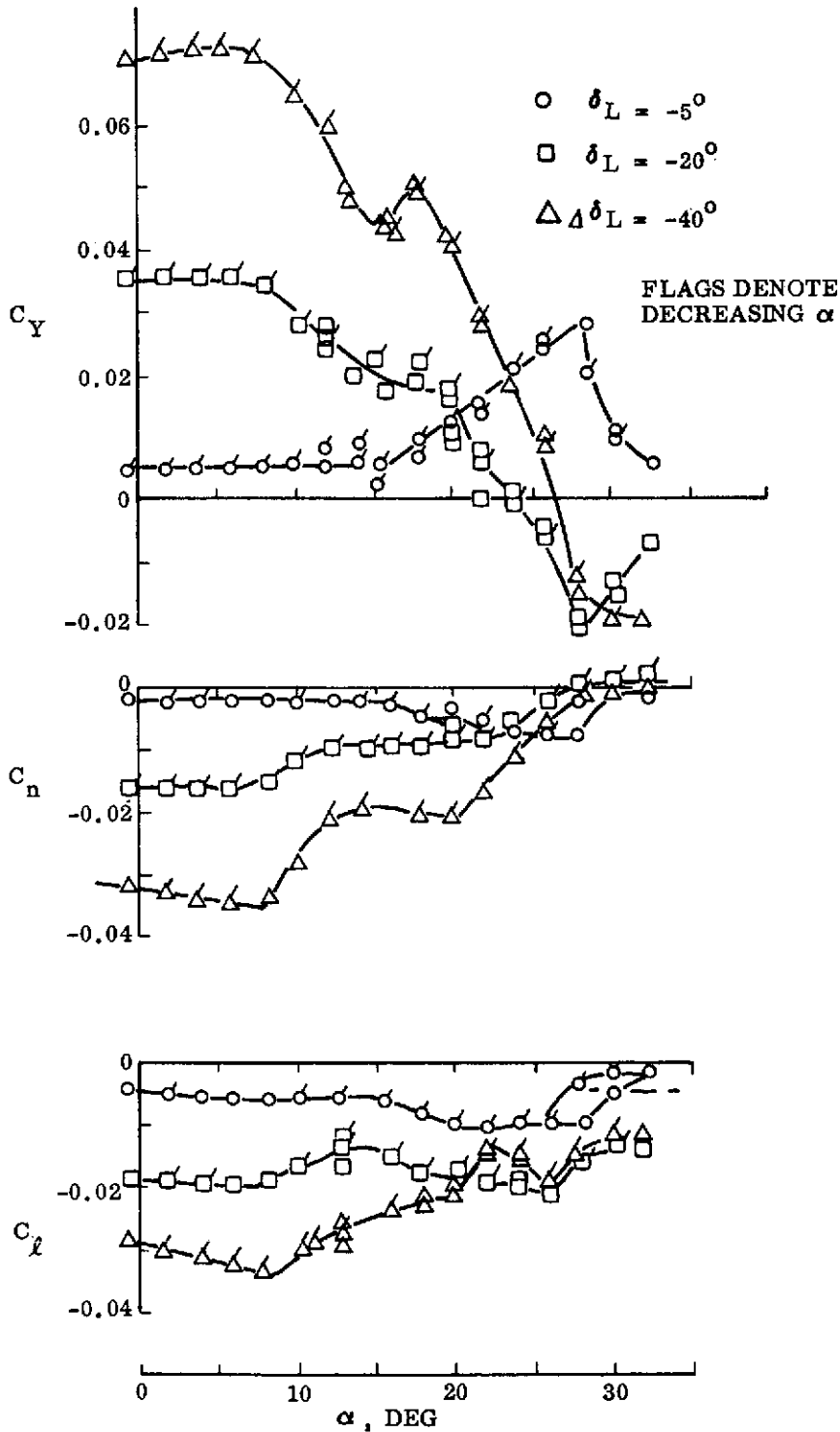
After passing through the region of shock-induced separation, the orbiter must negotiate a region of sudden leading edge stall. This boundary was predicted by assuming that the straight wing data of Ref. 3 could be applied to the delta wing when conditions normal to the leading edge are the same. In other words, it was assumed that sudden stall occurred when the angle of attack and Mach number normal to the delta wing leading edge (α_N and M_N , respectively) corresponded to the sudden stall condition in Ref. 3 $\left[\alpha_N = \tan^{-1} (\tan \alpha / \cos \Lambda) \text{ and } M_N = M_\infty \cos \Lambda (1 + \sin^2 \alpha \tan^2 \Lambda)^{1/2} \right]$. This may not be entirely true, because the spanwise flow component will alter the boundaries just as it did for the occurrence of the leading edge vortex. However, the present orbiter will experience sudden stall even if it does not occur exactly where predicted. It is likely that the orbiter will have some yaw or roll when traversing the sudden stall region, especially if it has just experienced roll undamping when traversing the region of shock-induced separation. Thus, sudden stall is likely to occur first on one wing, and snap roll similar to that experienced by the straight wing orbiter (Ref. 12) could result. The strake will not experience sudden stall because the orbiter angle of attack is too high.

At low subsonic speeds, it is doubtful that the 45° swept wing will develop a leading edge vortex, judging by experimental results (Ref. 13). For the borderline case of a 50° swept delta wing (Ref. 14), the formation of a leading edge vortex may be enhanced by a local strong shock at transonic speeds (Ref. 15). Thus, whether there is a leading edge vortex on the wing or not must be determined experimentally. The strake will certainly develop a leading edge vortex at subsonic speeds. The orbiter angle of attack is so high that a leading edge vortex will exist also at supersonic and hypersonic speeds. Recent unpublished oilflow results verify this (Fig. 19). The strake vortex generates lift on the wing as well as on the strake (Refs. 16 and 17). Thus, the stability characteristics will be vortex-dependent, and is desirable to avoid breakdown

of the strake vortex. Vortex burst is rather unlikely at subsonic speeds as long as the elevon deflection and yaw angle are small. The data of Ref. 7 shows that for a pure 80° delta wing, vortex burst occurs at the orbiter trailing edge at $\alpha = 37.5^\circ$ (Fig. 20). Thus, vortex burst is unlikely to endanger the shuttle flying at $\alpha = 10^\circ$.

Elevon deflection could possibly cause a significant enough change in the subsonic burst attitude to affect the orbiter, especially if the yaw angle were significant. It has been shown that an obstacle in the wake of a delta wing can induce burst (Ref. 5). An upward elevon deflection (minus δ) can in a similar manner promote vortex burst, as the current test demonstrates. This elevon-induced burst will be very sensitive to sideslip. Because it is planned to trim the shuttle with leeward elevon deflections to minimize control surface heating, this is an area of serious concern. Burst is highly undesirable because it can cause sudden discontinuous changes in pitch, roll, and yaw stability, often associated with hysteresis effects (see Ref. 8 and present test data).

Even though the new orbiter is somewhat different from the 040A, it retains the configuration characteristics that are responsible for the discontinuous yaw derivatives, i. e., large leeward elevon deflections, a relatively large fuselage, and large OMS pods. It is possible, then, that similar effects could occur on the new orbiter. Thus, it appears that the current orbiter will be subject to the same unsteady flow phenomena that plagued earlier configurations, although they will occur during different times in the entry trajectory and their seriousness relative to the vehicle dynamics may be quite different.



a. LATERAL-DIRECTIONAL CHARACTERISTICS

Figure 3. 040A Orbiter Pitch Stability at M = 0.9 (Sheet 1 of 2)

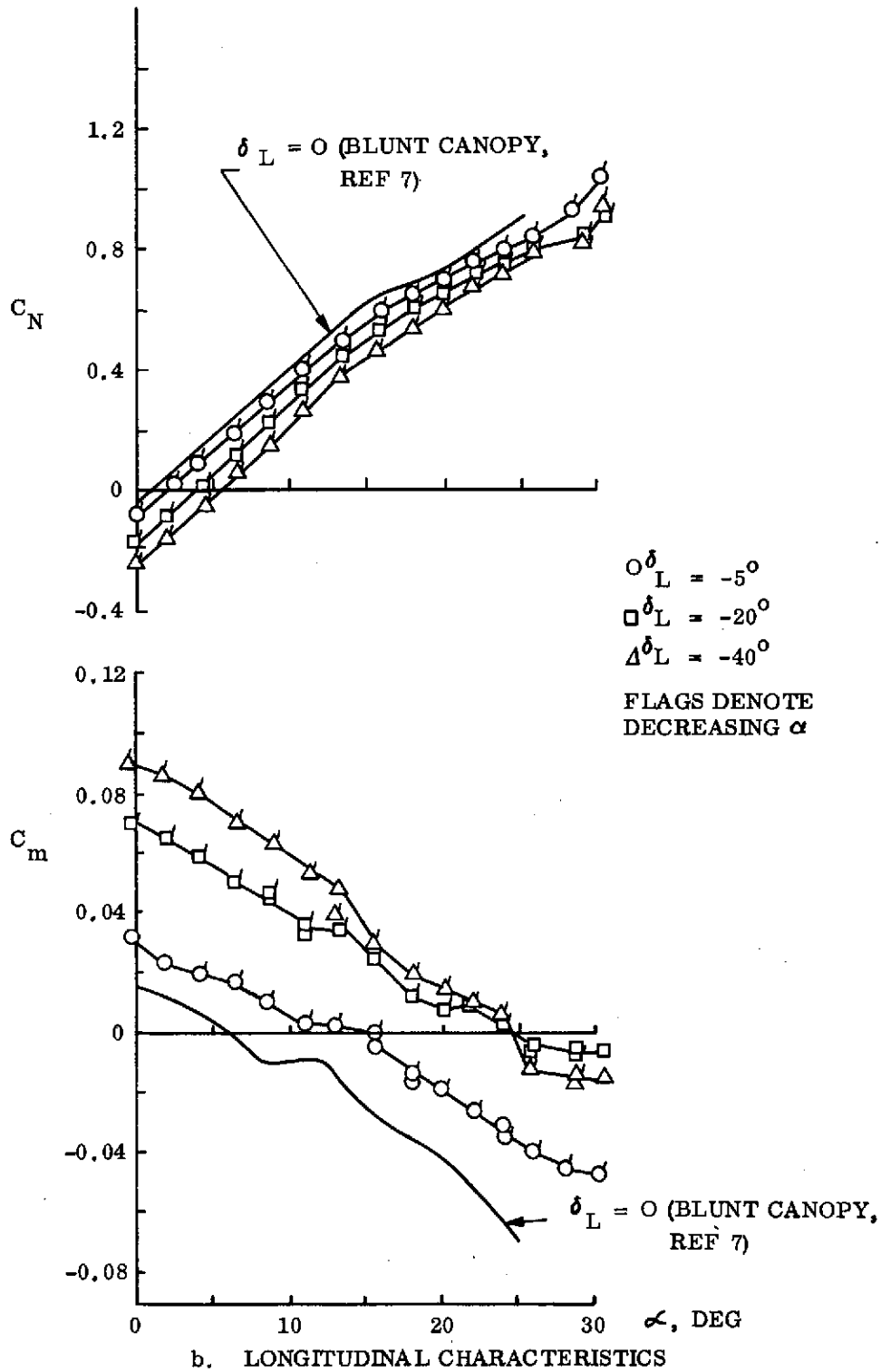
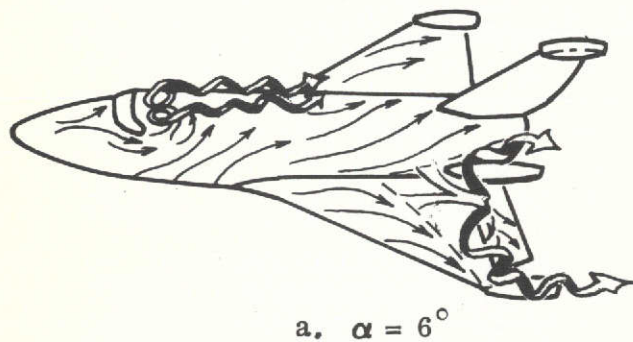
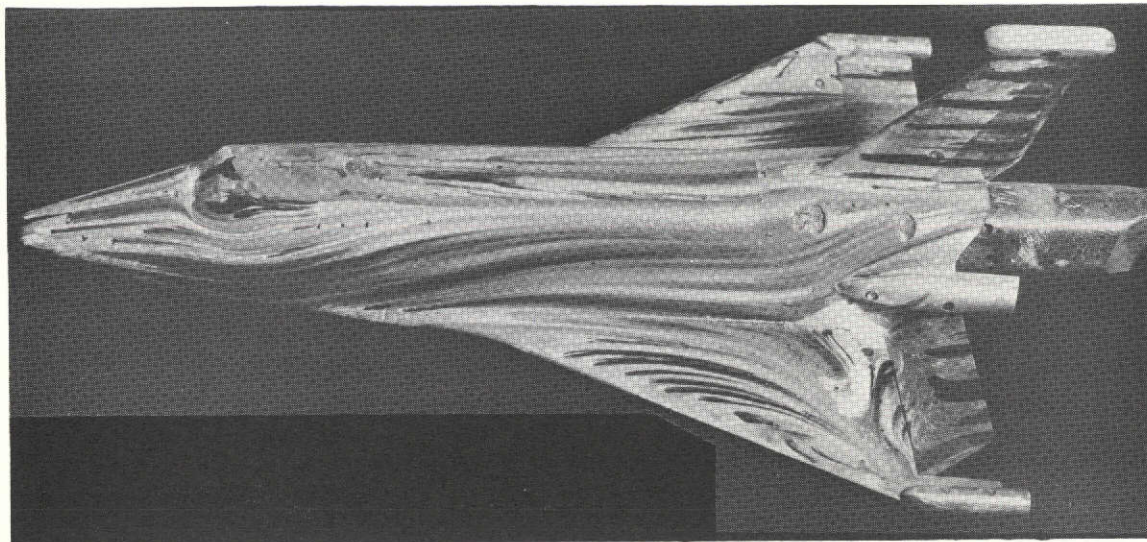


Figure 3. 040A Orbiter Pitch Stability at M = 0.9 (Sheet 2 of 2)



⇨ LIFTED STREAMLINE
⇨ SURFACE STREAMLINE

a. $\alpha = 6^\circ$

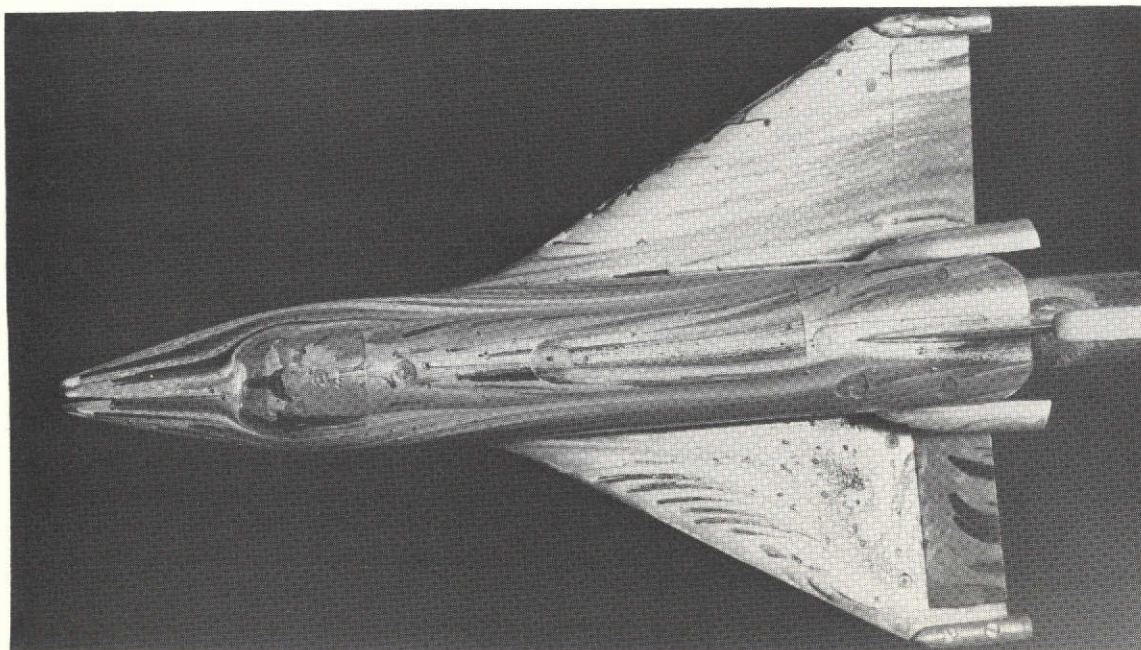
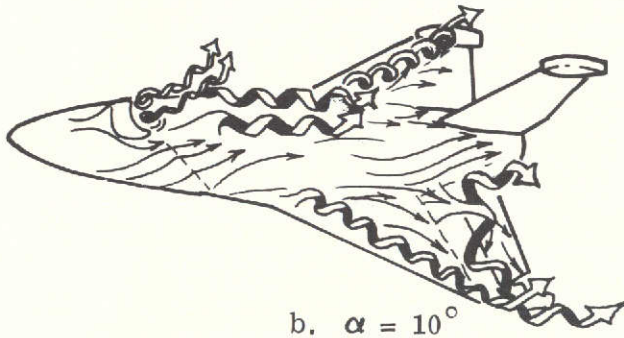
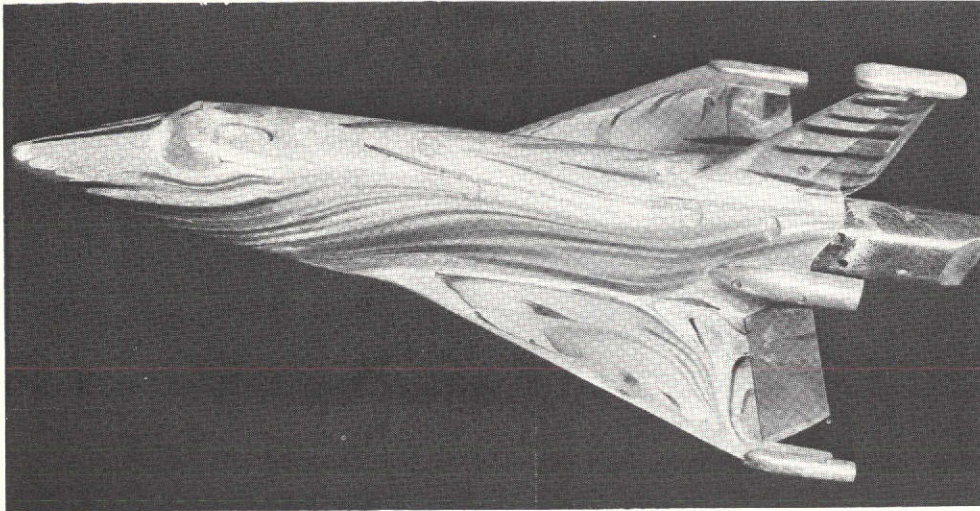
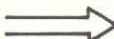



Figure 4. 040A Orbiter Surface Flow Patterns,
 $M = 0.9$, $\delta_L = -40^\circ$, $\delta_R = 0$ (Sheet 1 of 5)



 LIFTED STREAMLINE
 SURFACE STREAMLINE

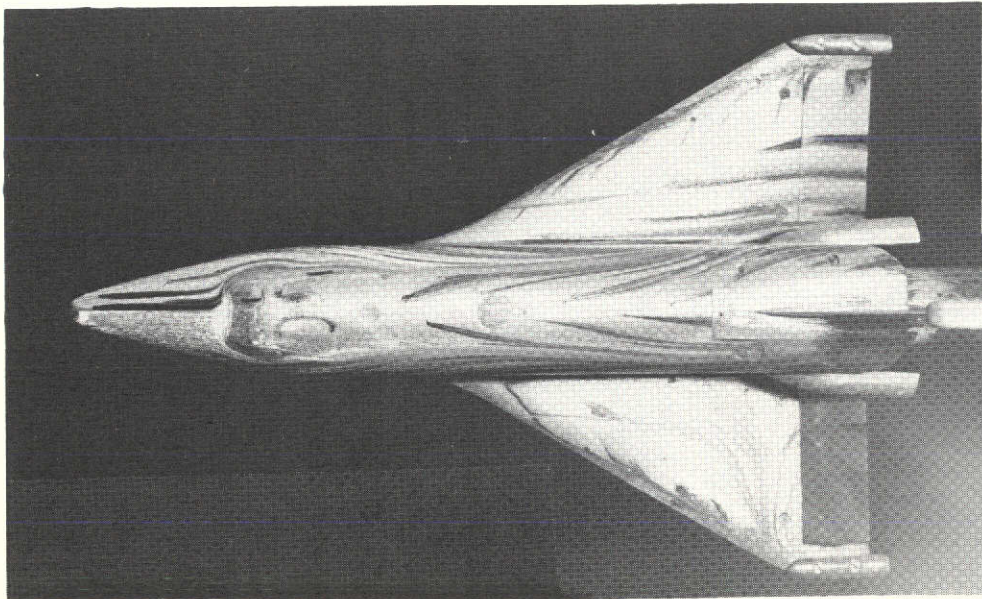


Figure 4. 040A Orbiter Surface Flow Patterns,
 $M = 0.9$, $\delta_L = -40^\circ$, $\delta_R = 0$ (Sheet 2 of 5)

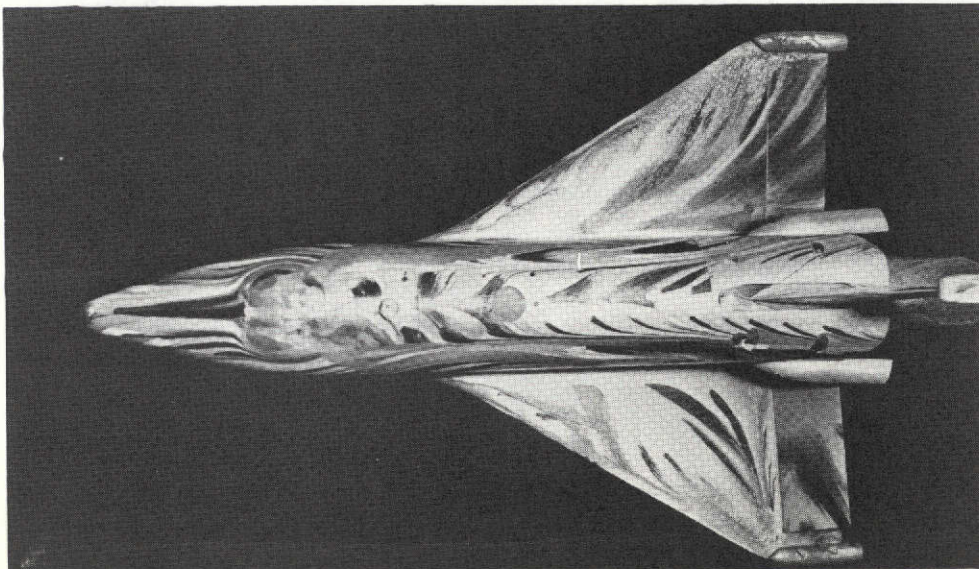
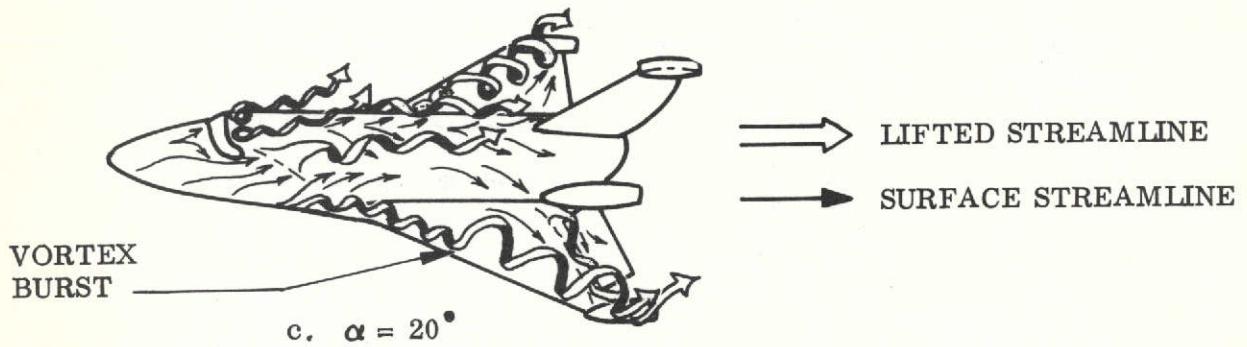
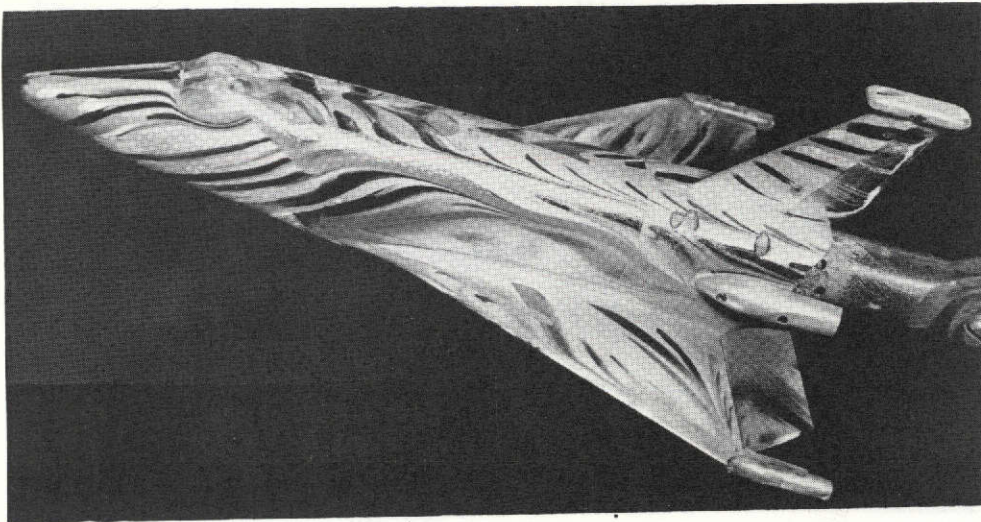
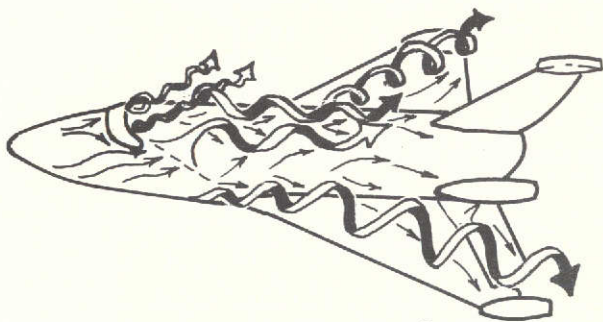
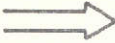



Figure 4. 040A Orbiter Surface Flow Patterns,
 $M = 0.9$, $\delta_L = -40^\circ$, $\delta_R = 0$ (Sheet 3 of 5)



 LIFTED STREAMLINE
 SURFACE STREAMLINE

d. $\alpha = 24^\circ$

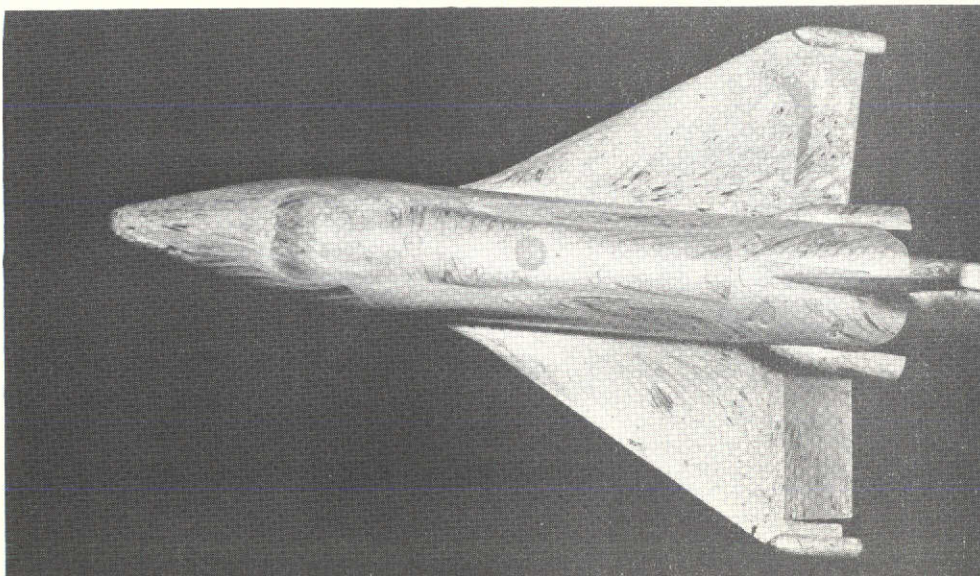
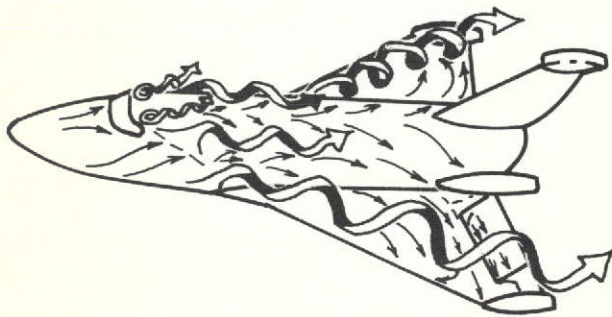
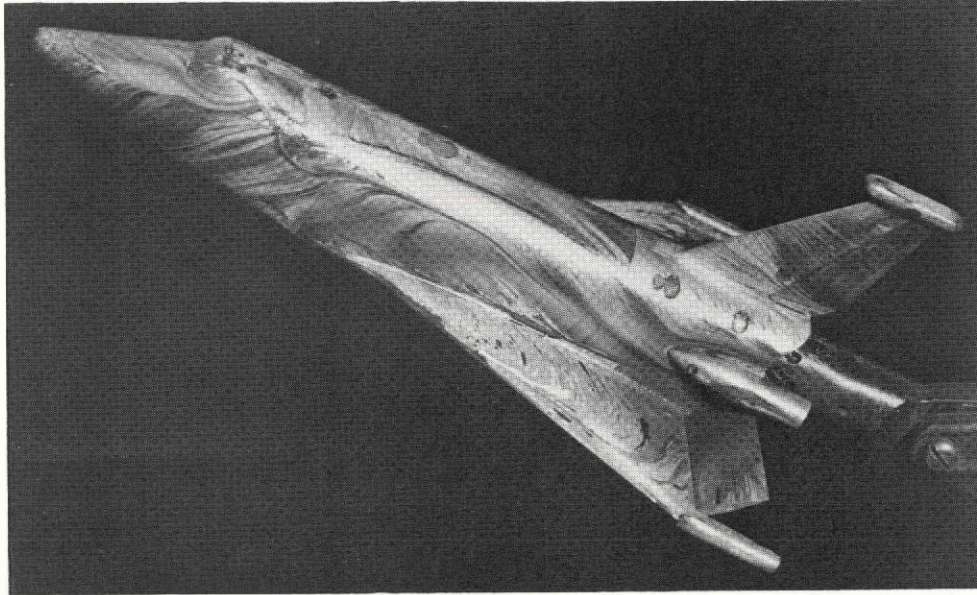


Figure 4. 040A Orbiter Surface Flow Patterns,
 $M = 0.9$, $\delta_L = -40^\circ$, $\delta_R = 0$ (Sheet 4 of 5)



⇨ LIFTED STREAMLINE
⇨ SURFACE STREAMLINE

e. $\alpha = 30^\circ$

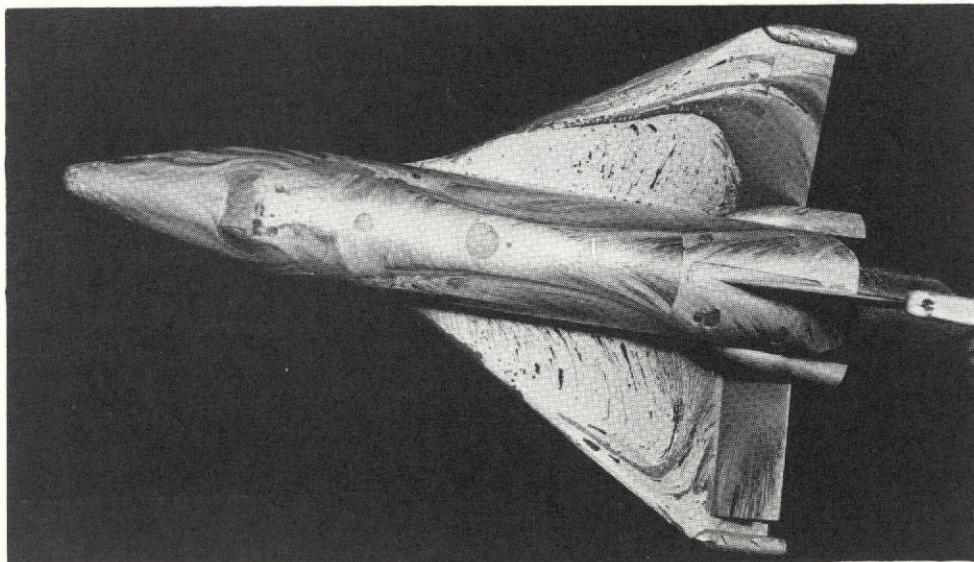


Figure 4. 040A Orbiter Surface Flow Patterns,
 $M = 0.9$, $\delta_L = -40^\circ$, $\delta_R = 0$ (Sheet 5 of 5)

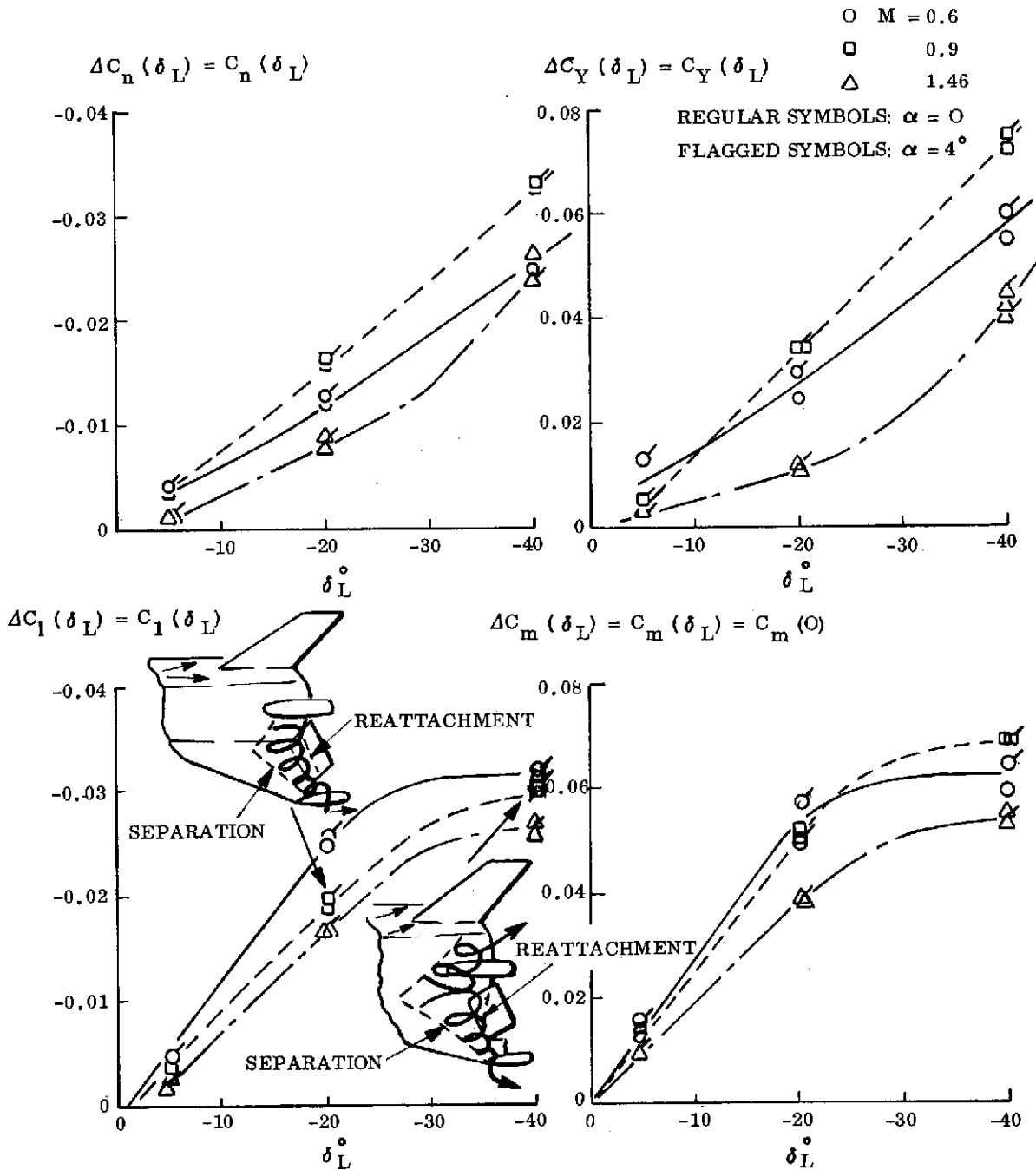
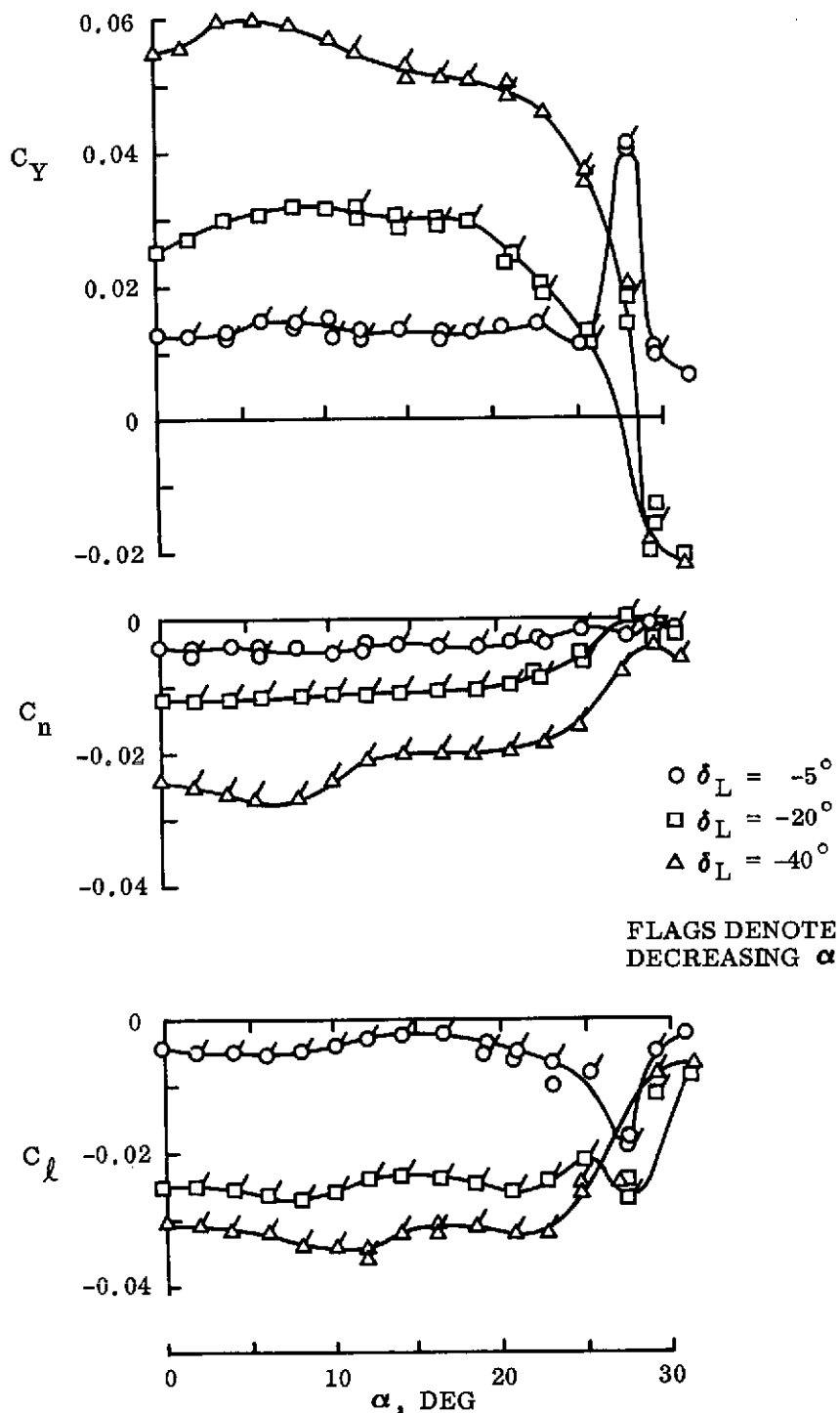
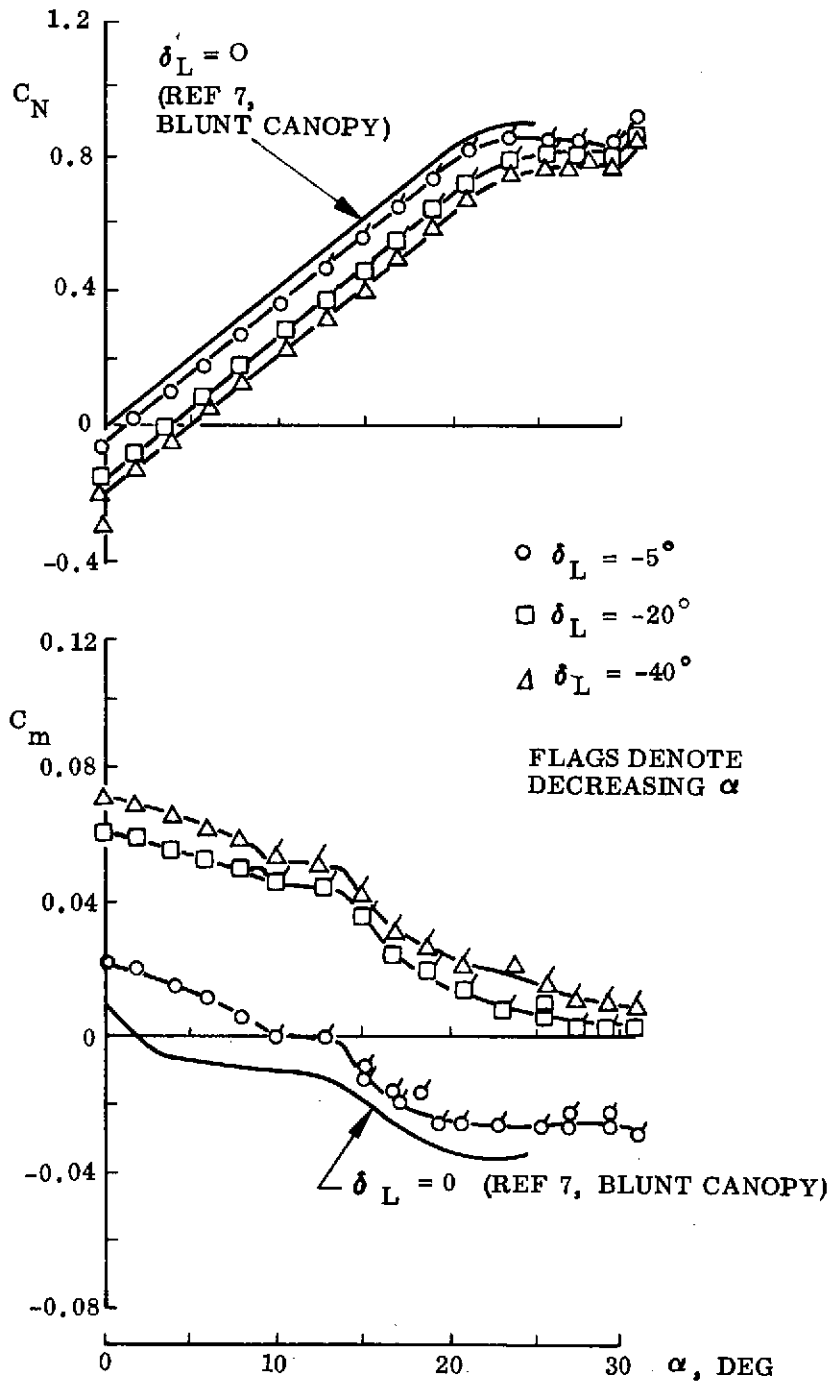


Figure 5. 040A Orbiter Elevon Control Effectiveness



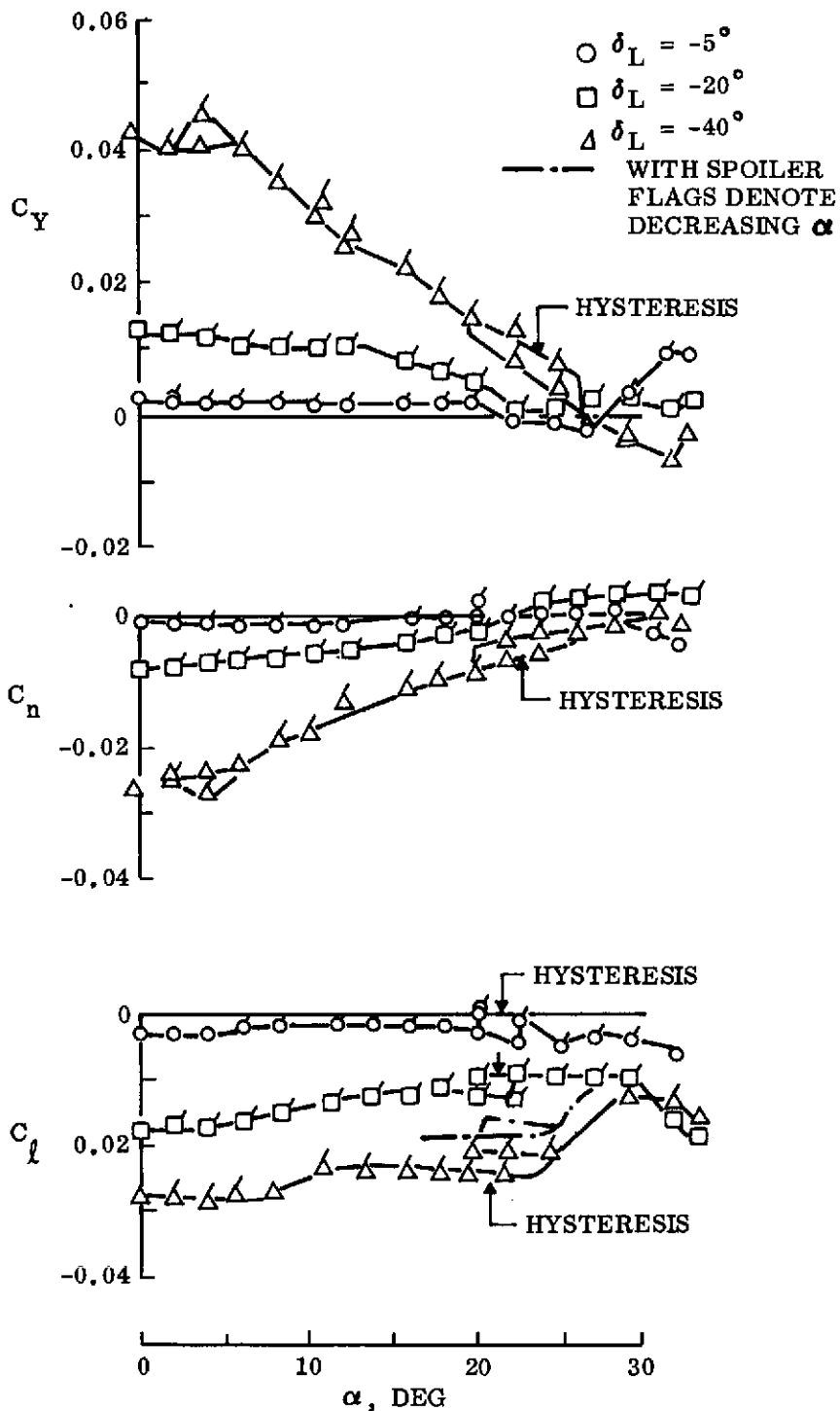
a. LATERAL-DIRECTIONAL CHARACTERISTICS

Figure 6. 040A Orbiter Pitch Stability at M = 0.6
(Sheet 1 of 2)



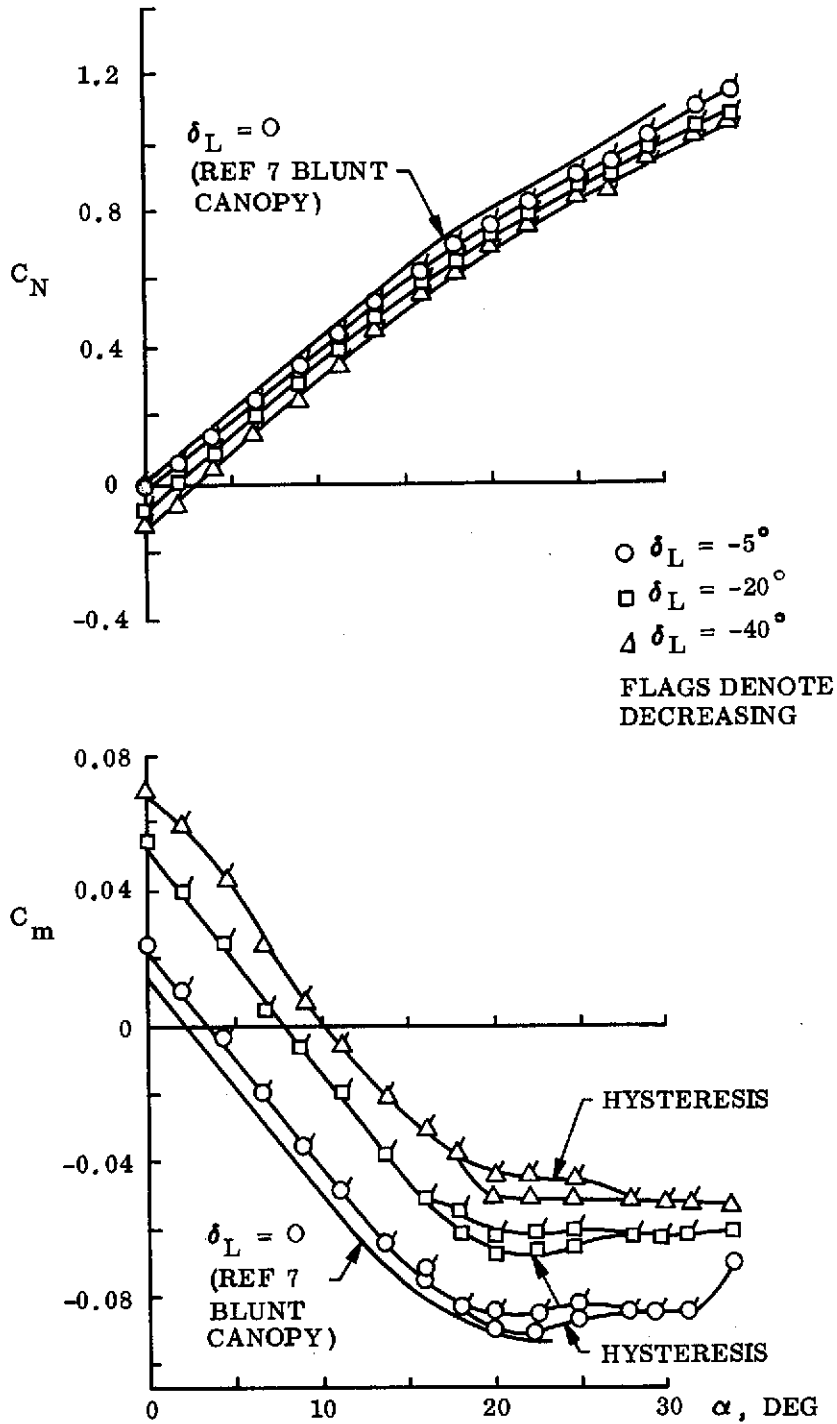
b LONGITUDINAL CHARACTERISTICS

Figure 6. 040A Orbiter Pitch Stability at M = 0.6
(Sheet 2 of 2)



a. LATERAL - DIRECTIONAL CHARACTERISTICS

Figure 7. 040A Orbiter Pitch Stability at M = 1.46
(Sheet 1 of 2)



b. LONGITUDINAL CHARACTERISTICS

Figure 7. 040A Orbiter Pitch Stability at M = 1.46
(Sheet 2 of 2)

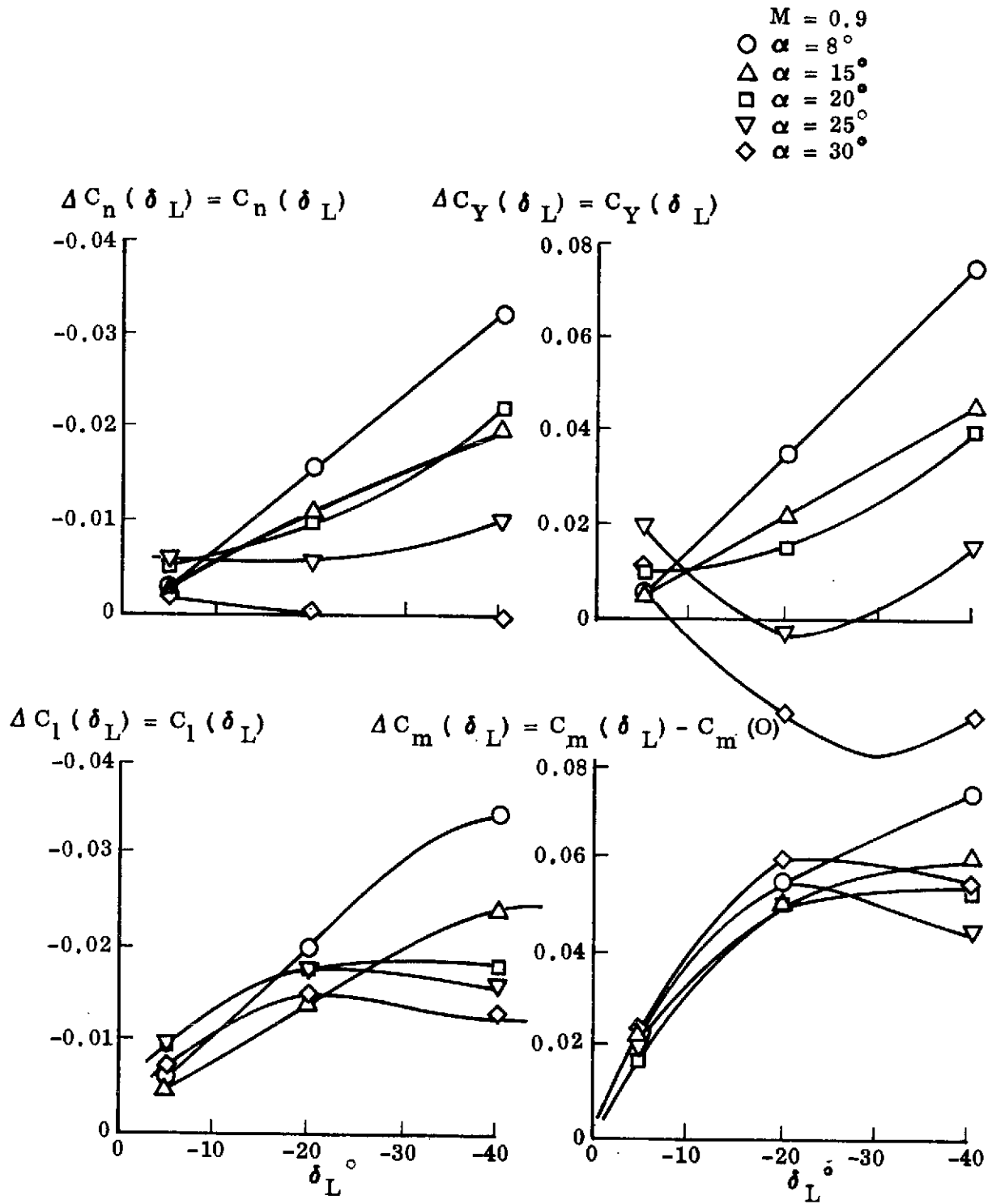
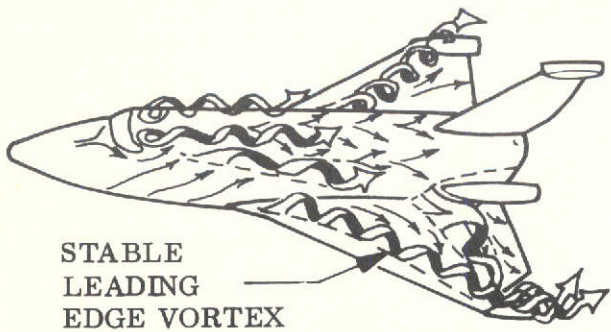
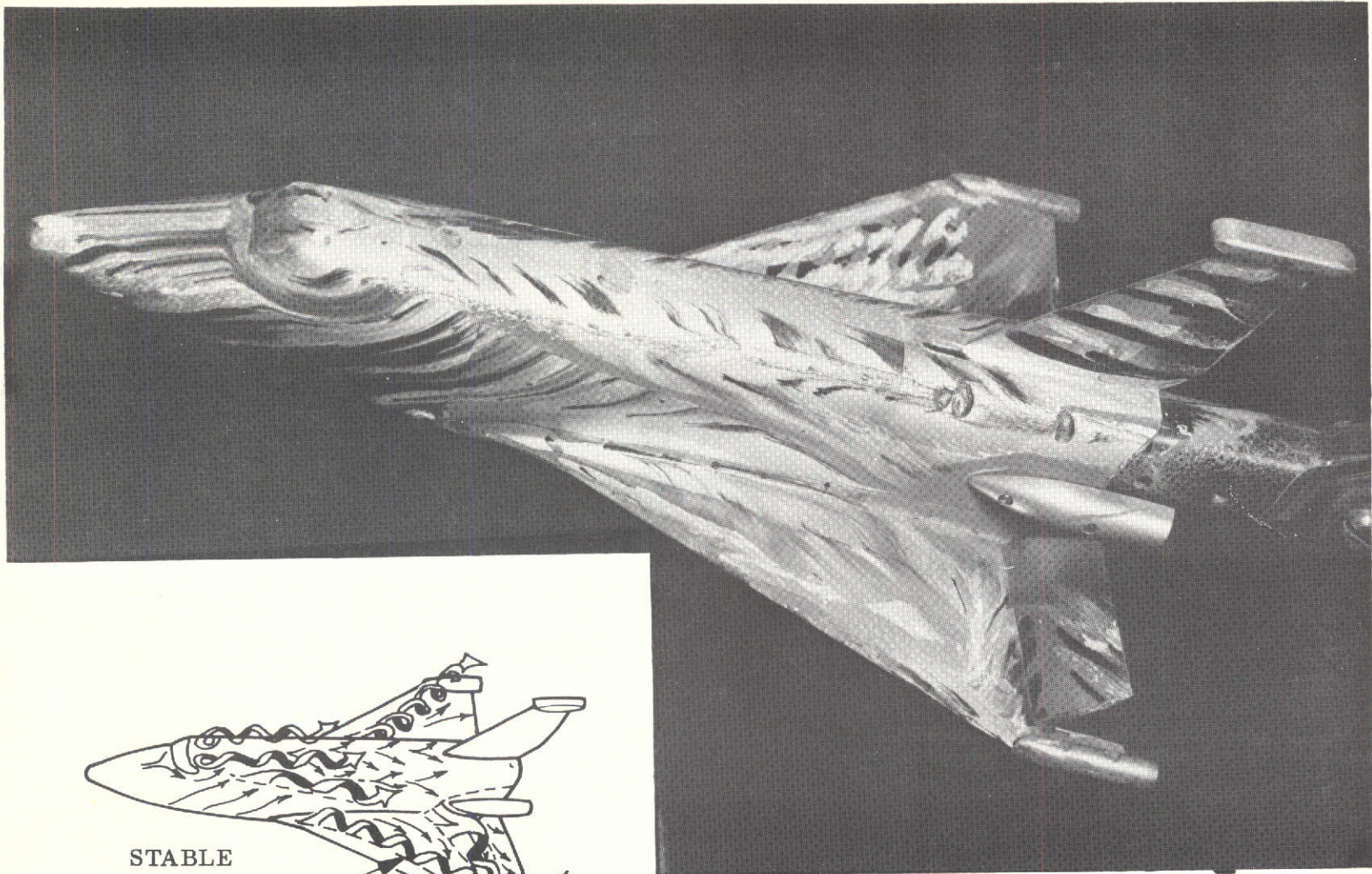


Figure 8. 040A Orbiter Elevon Control Characteristics at M = 0.9

3-27



a. α INCREASING

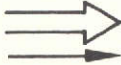
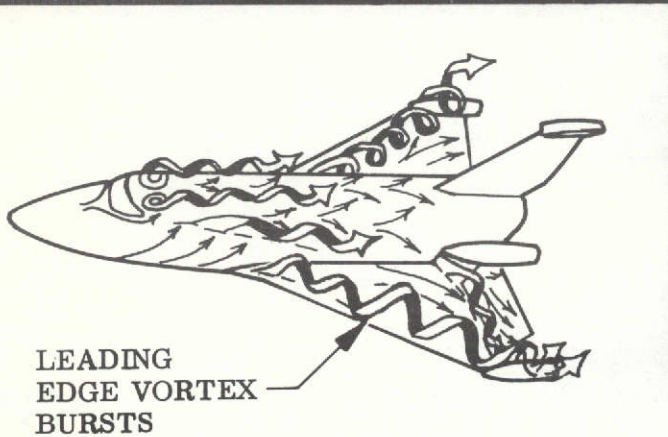
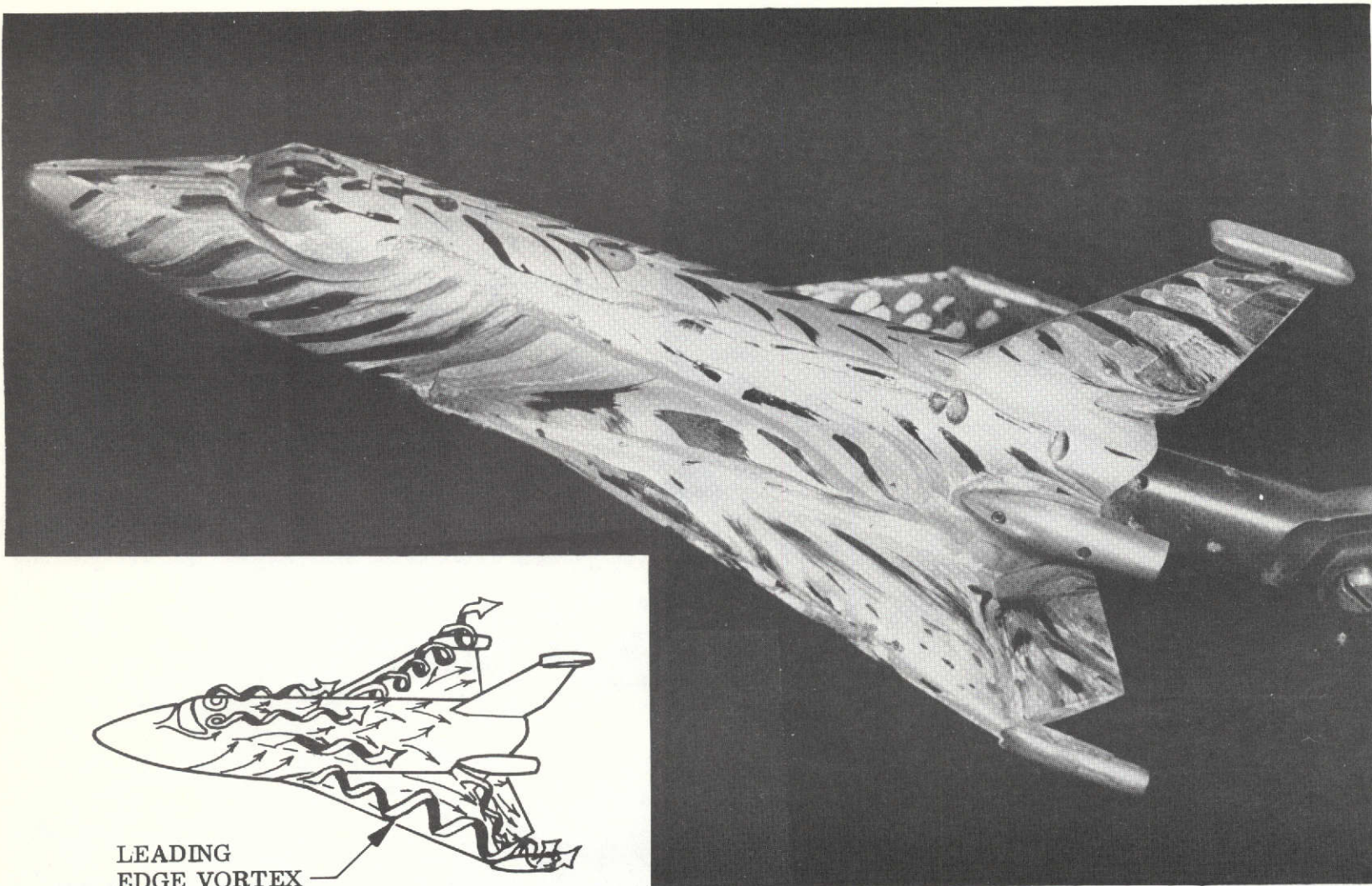

 LIFTED STREAMLINE
 SURFACES STREAMLINE

Figure 9. 040A Orbiter Surface Flow Patterns in α Hysteresis Region;
 $M = 1.46$, $\alpha = 22^\circ$, $\delta_L = -40^\circ$, $\delta_R = 0$ (Sheet 1 of 3)

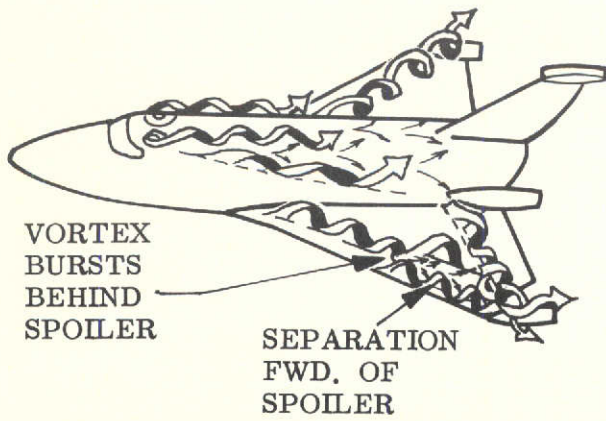
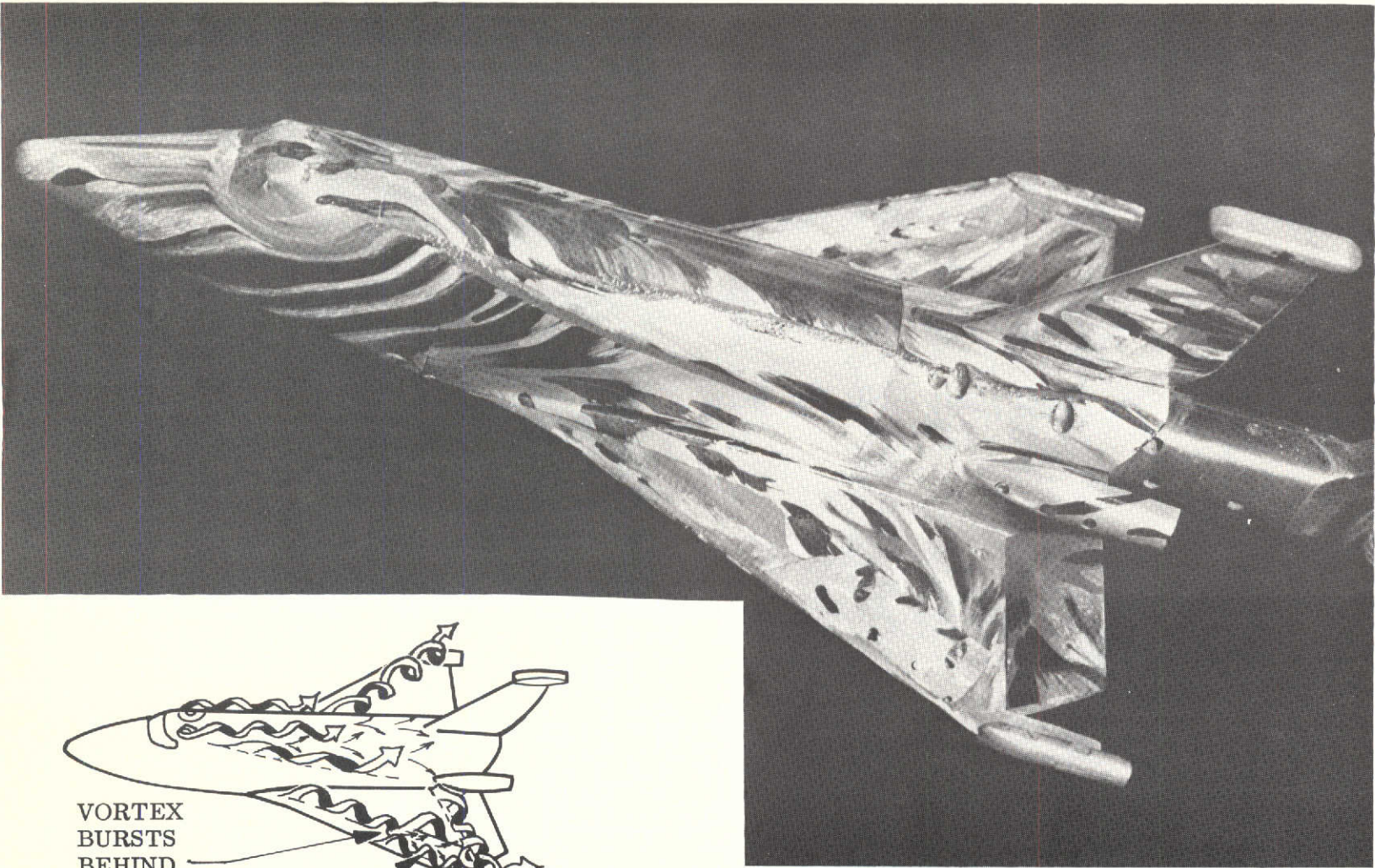


b. α DECREASING

 LIFTED STREAMLINE
 SURFACES STREAMLINE

Figure 9. 040A Orbiter Surface Flow Patterns in α Hysteresis Region;
 $M = 1.46$, $\alpha = 22^\circ$, $\delta_L = -40^\circ$, $\delta_R = 0$ (Sheet 2 of 3)

3-29



c. WITH SPOILER; α INCREASING



Figure 9. 040A Orbiter Surface Flow Patterns in α Hysteresis Region;

$M = 1.46$, $\alpha = 22^\circ$, $\delta_L = -40^\circ$, $\delta_R = 0$ (Sheet 3 of 3)

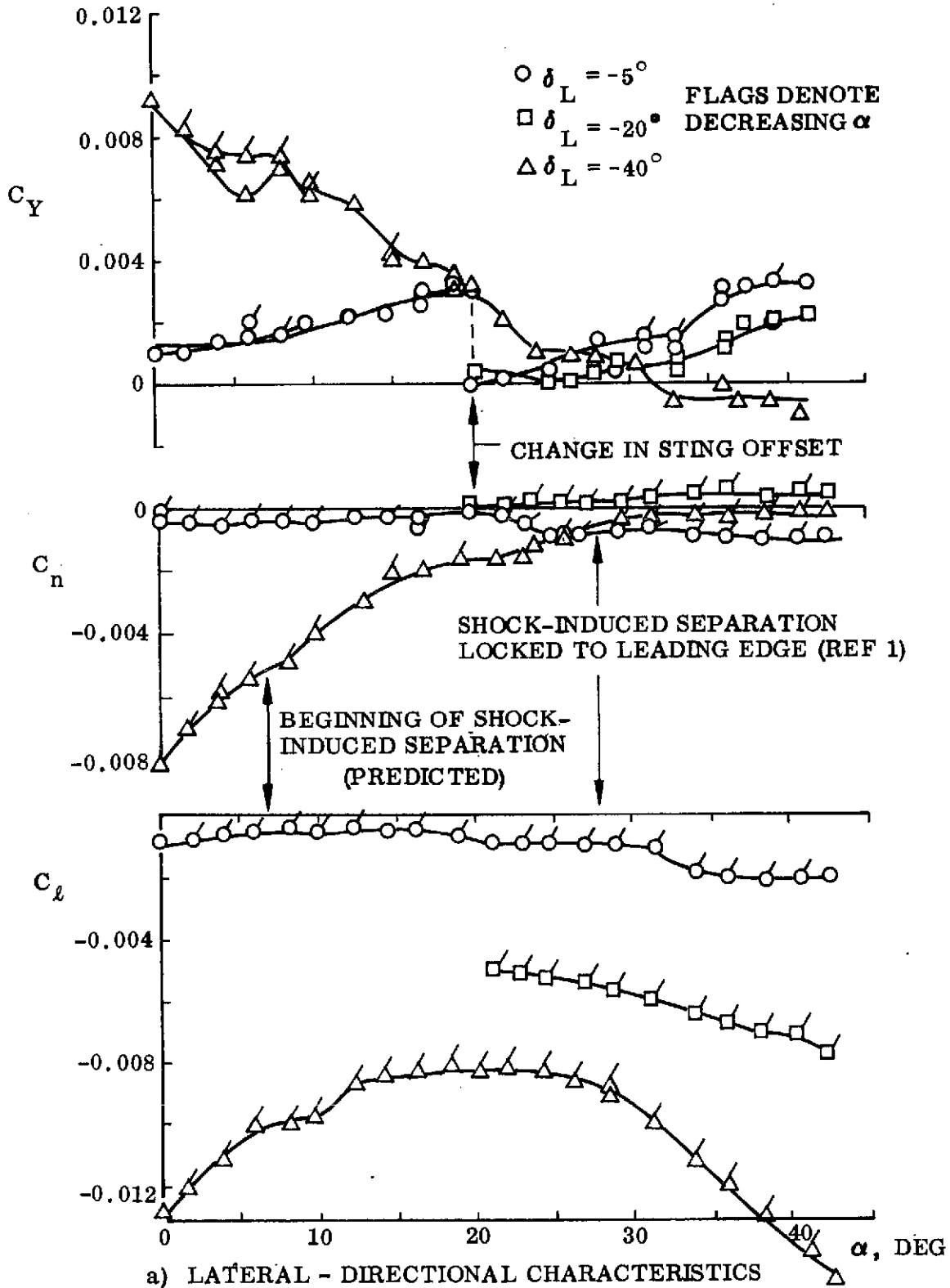
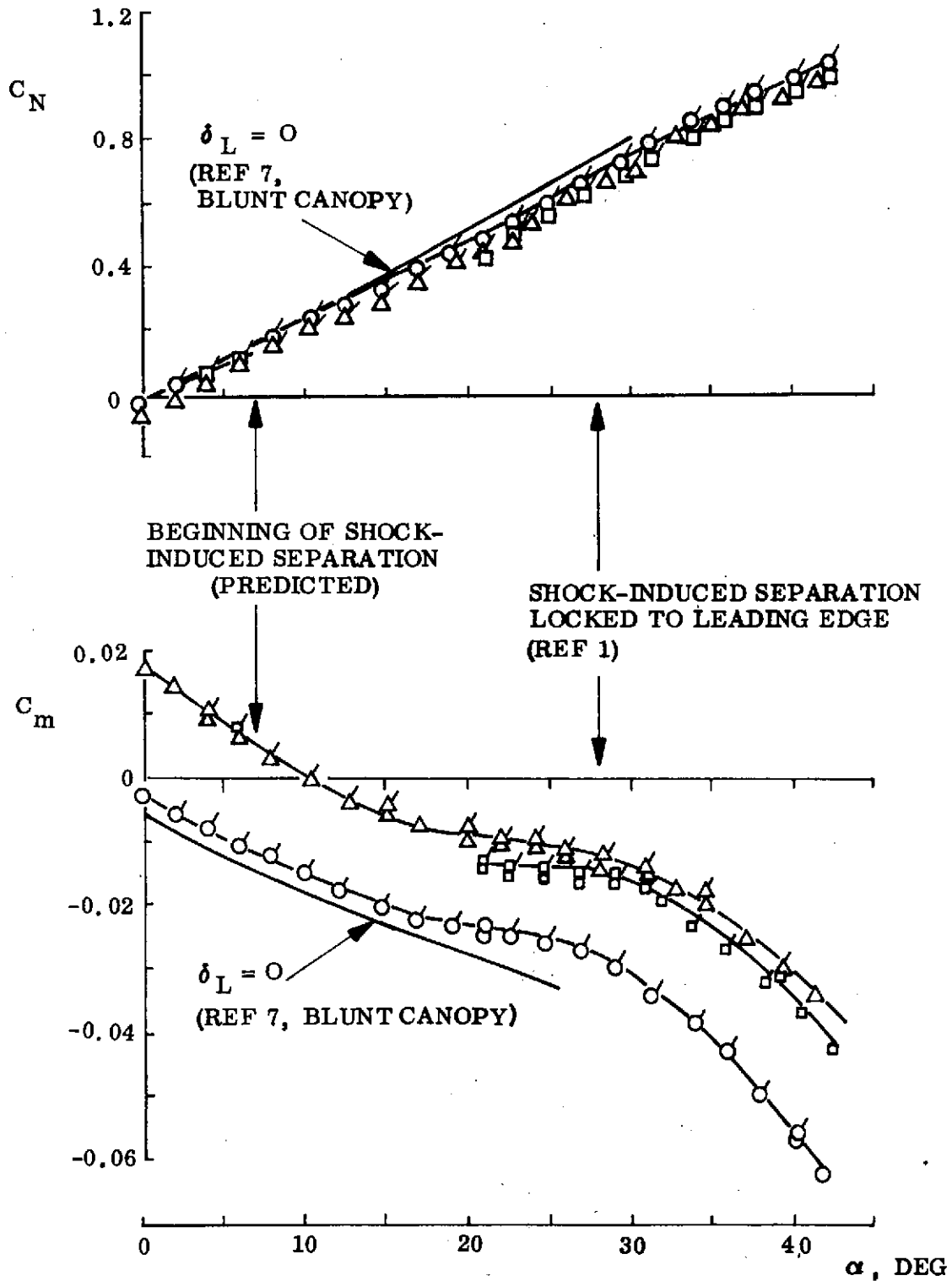
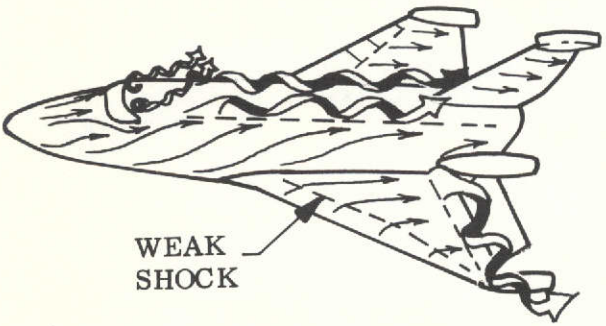
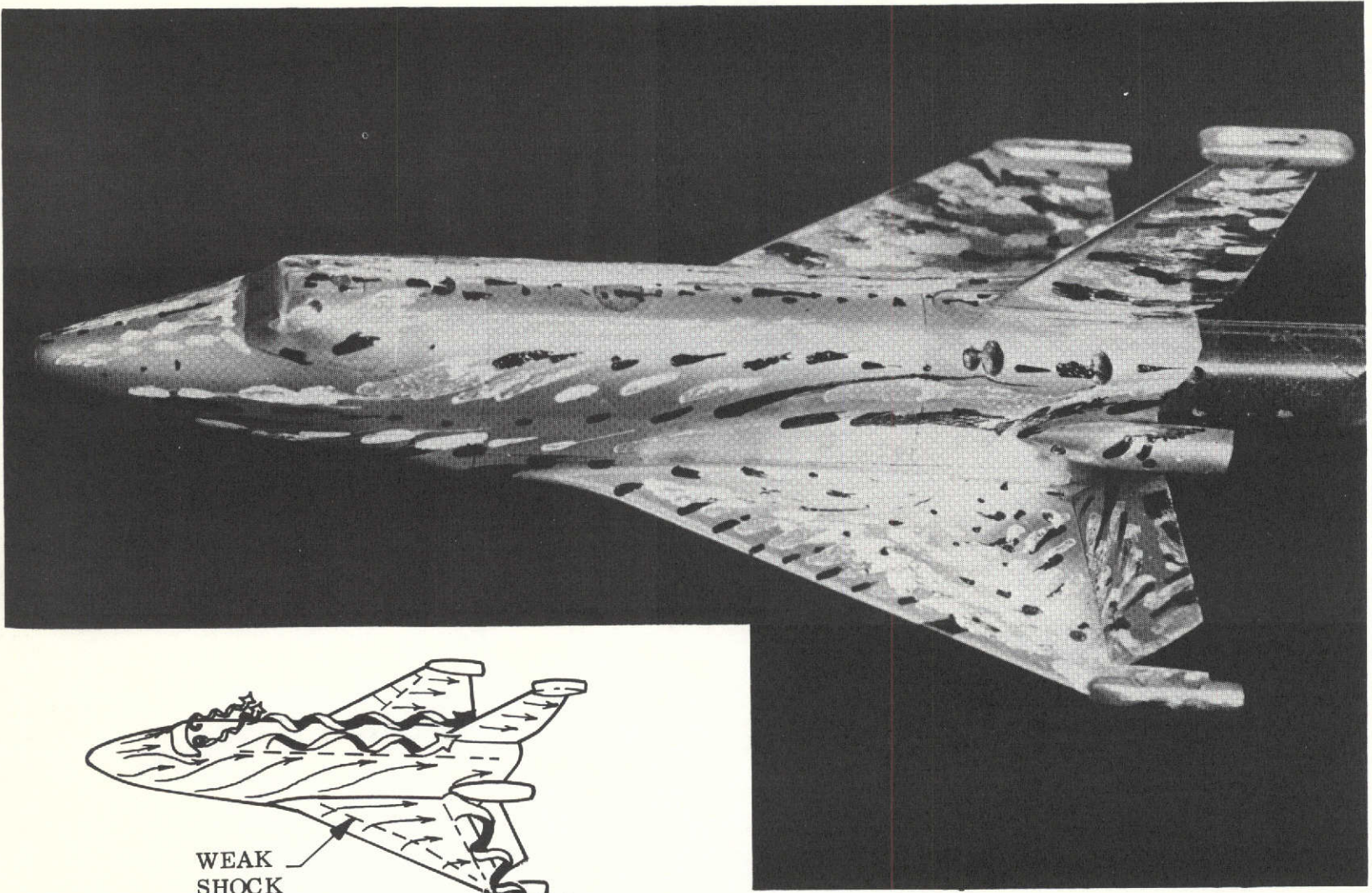


Figure 10. 040A Orbiter Pitch Stability at M = 2.99 (Sheet 1 of 2)



b. LONGITUDINAL CHARACTERISTICS

Figure 10. 040A Orbiter Pitch Stability at M = 2.99 (Sheet 2 of 2)



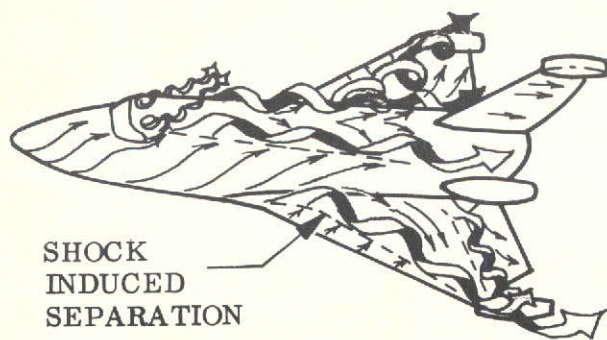
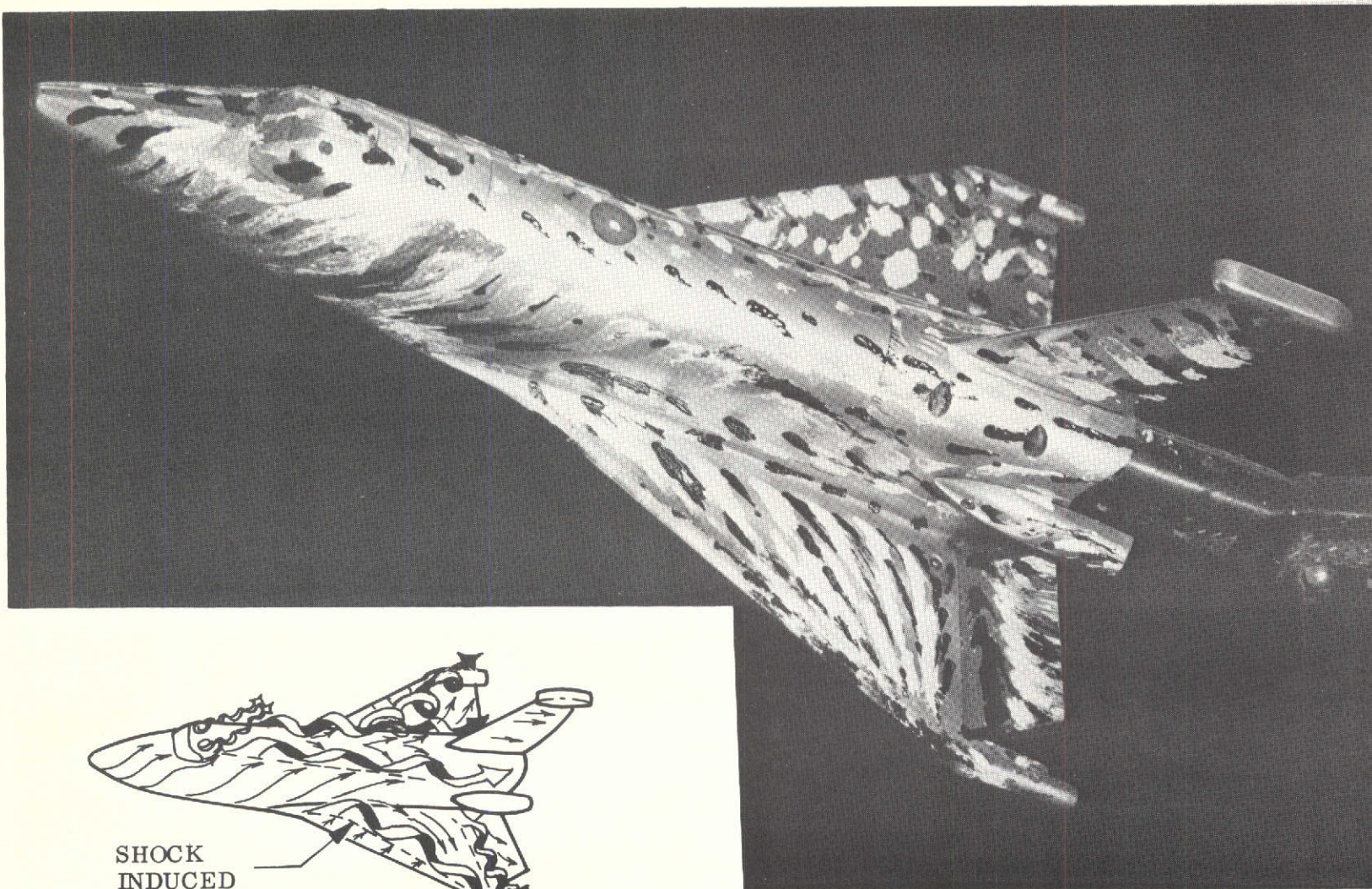
a. $\alpha = 6^\circ$

LIFTED STREAMLINE
 SURFACE STREAMLINE

Figure 11. 040A Orbiter Surface Flow Patterns; $M = 2.99$,
 $\delta_L = -40^\circ$, $\delta_R = 0$ (Sheet 1 of 3)

3-32

3-33

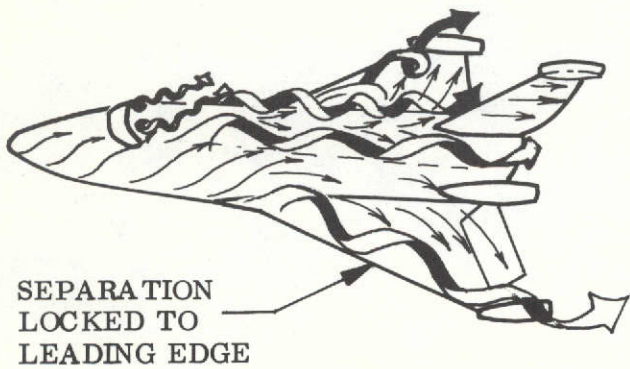
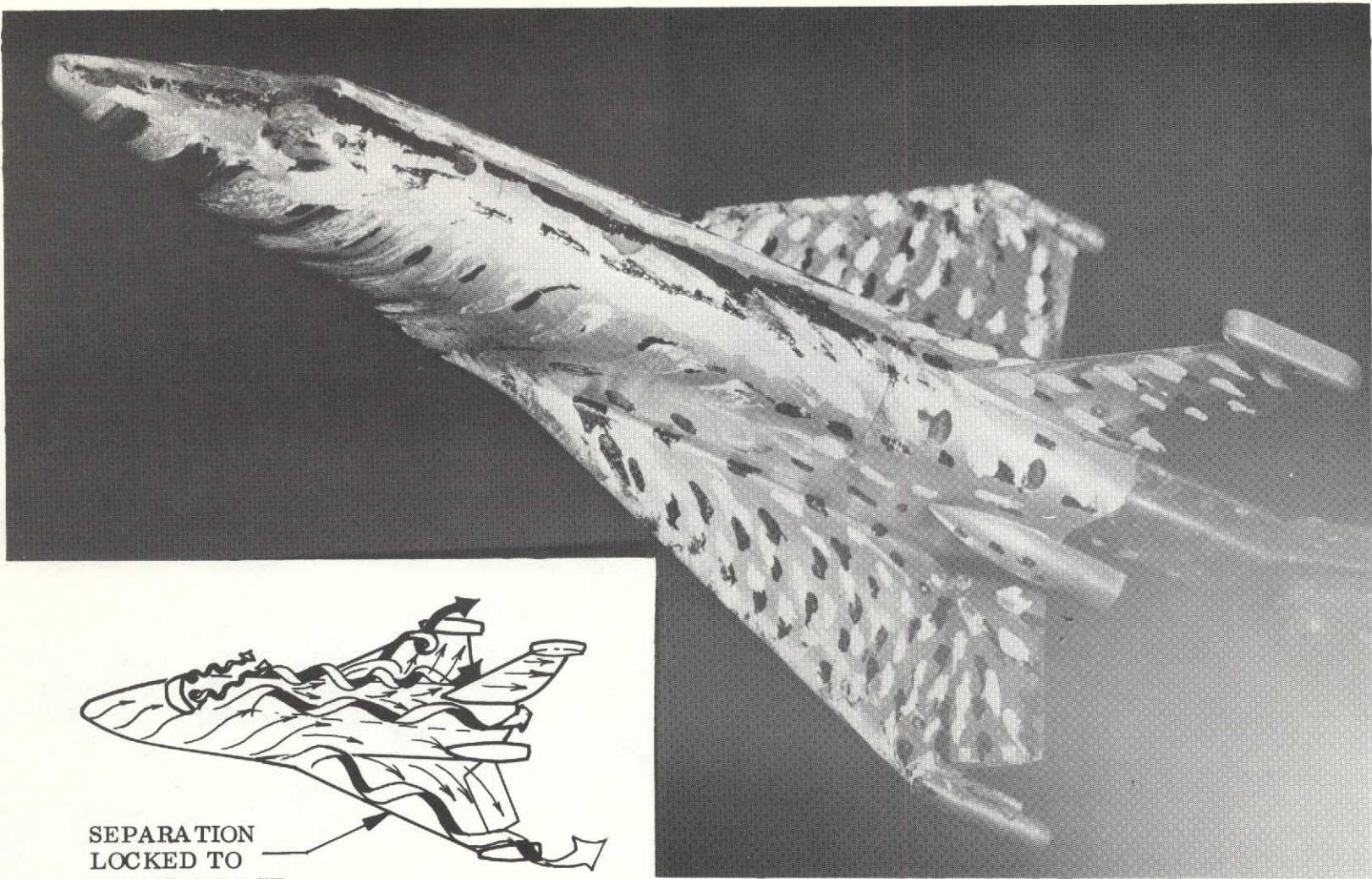


b. $\alpha = 14^\circ$

LIFTED STREAMLINE
 SURFACE STREAMLINE

Figure 11. 040A Orbiter Surface Flow Patterns; $M = 2.99$,

$\delta_L = -40^\circ$, $\delta_R = 0$ (Sheet 2 of 3)



c. $\alpha = 20^\circ$

LIFTED STREAMLINE
 SURFACE STREAMLINE

Figure 11. 040A Orbiter Surface Flow Patterns; $M = 2.99$,
 $\delta_L = -40^\circ$, $\delta_R = 0$ (Sheet 3 of 3)

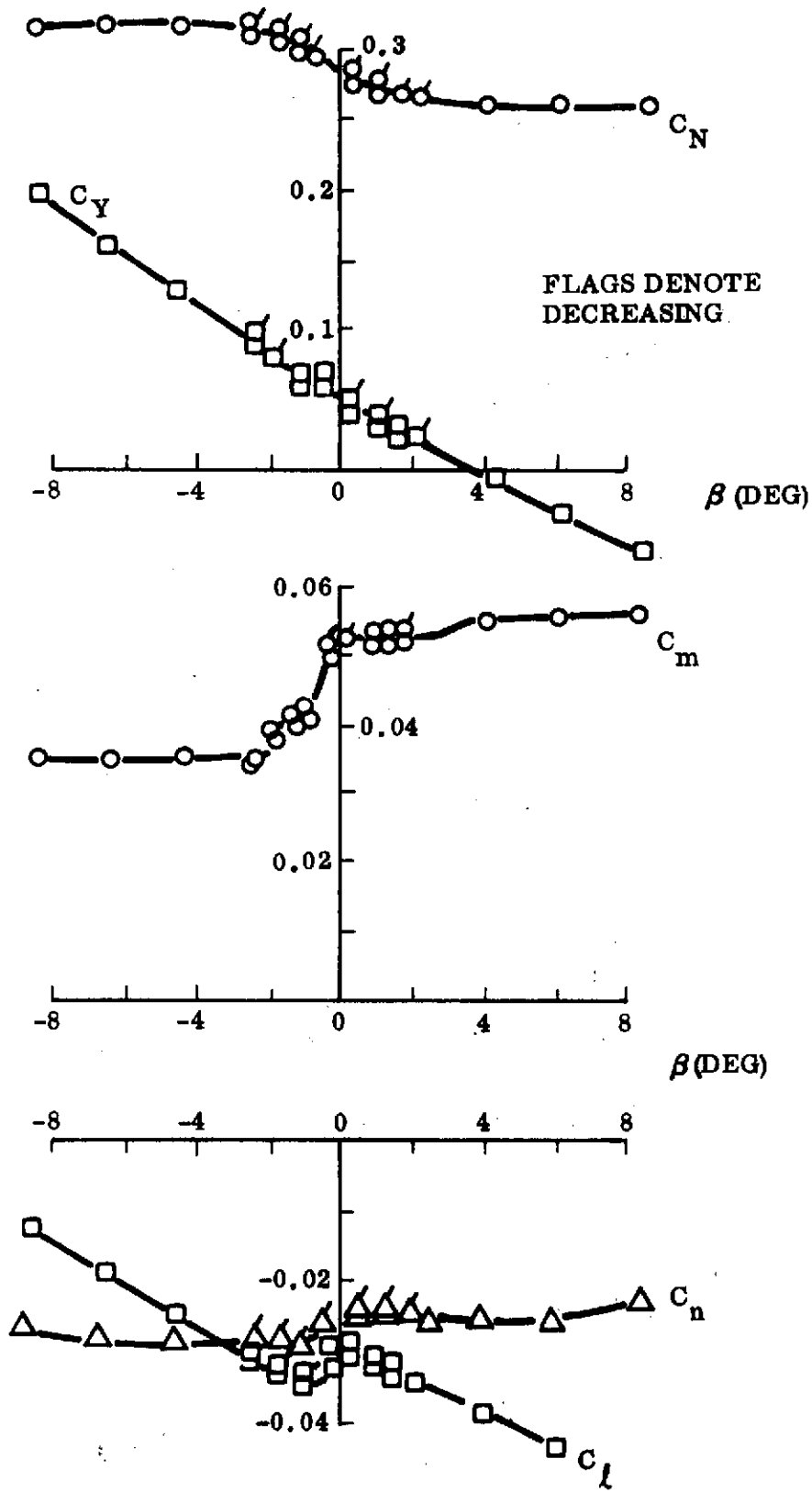


Figure 12. 040A Orbiter Yaw Stability;
 $M = 0.9$, $\alpha = 11^\circ$, $\delta_L = -40^\circ$, $\delta_R = 0$

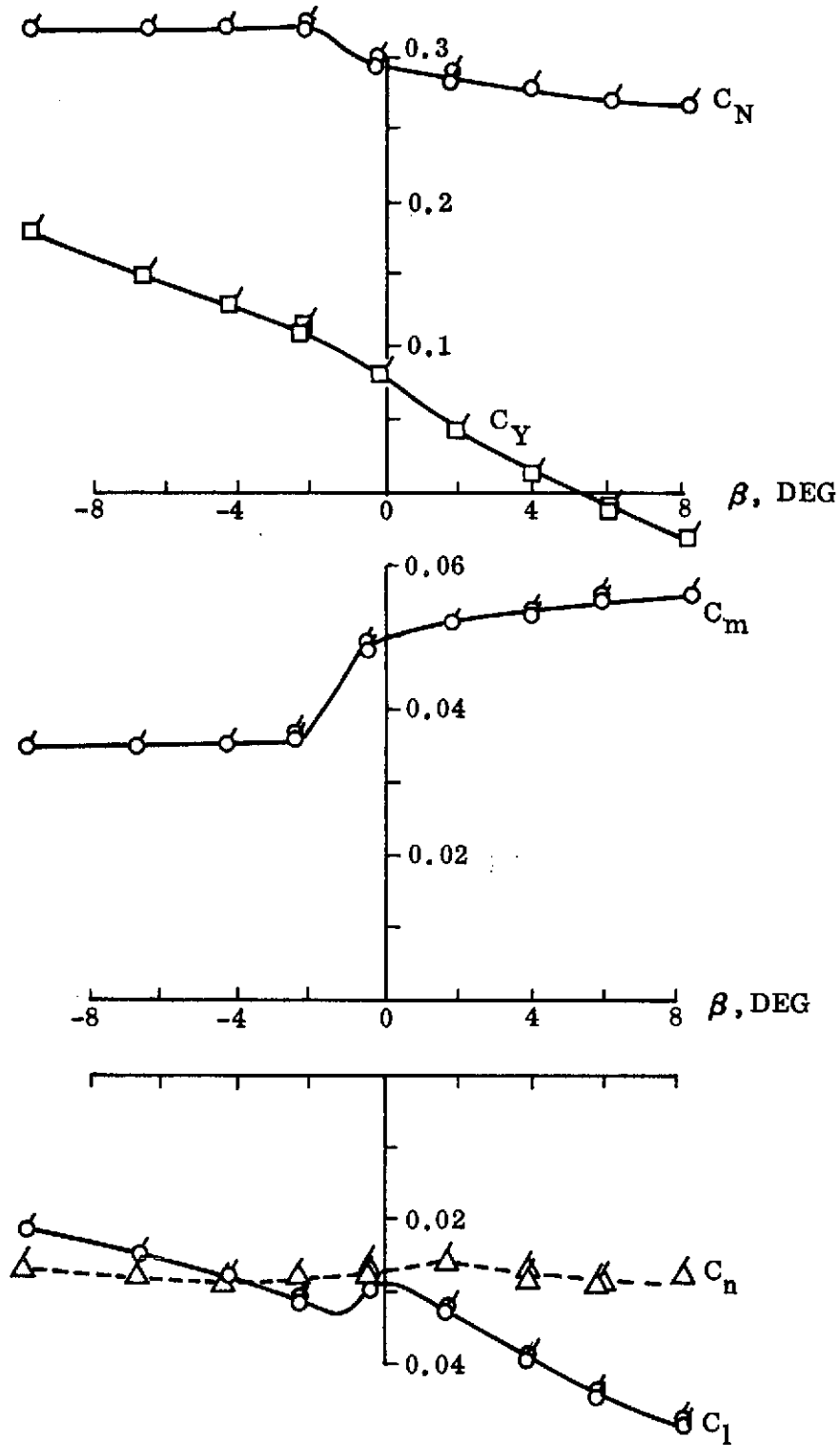


Figure 13. 040A Orbiter Yaw Stability;
 $M = 0.6$, $\alpha = 10.4^\circ$, $\delta_L = -40^\circ$, $\delta_R = 0$

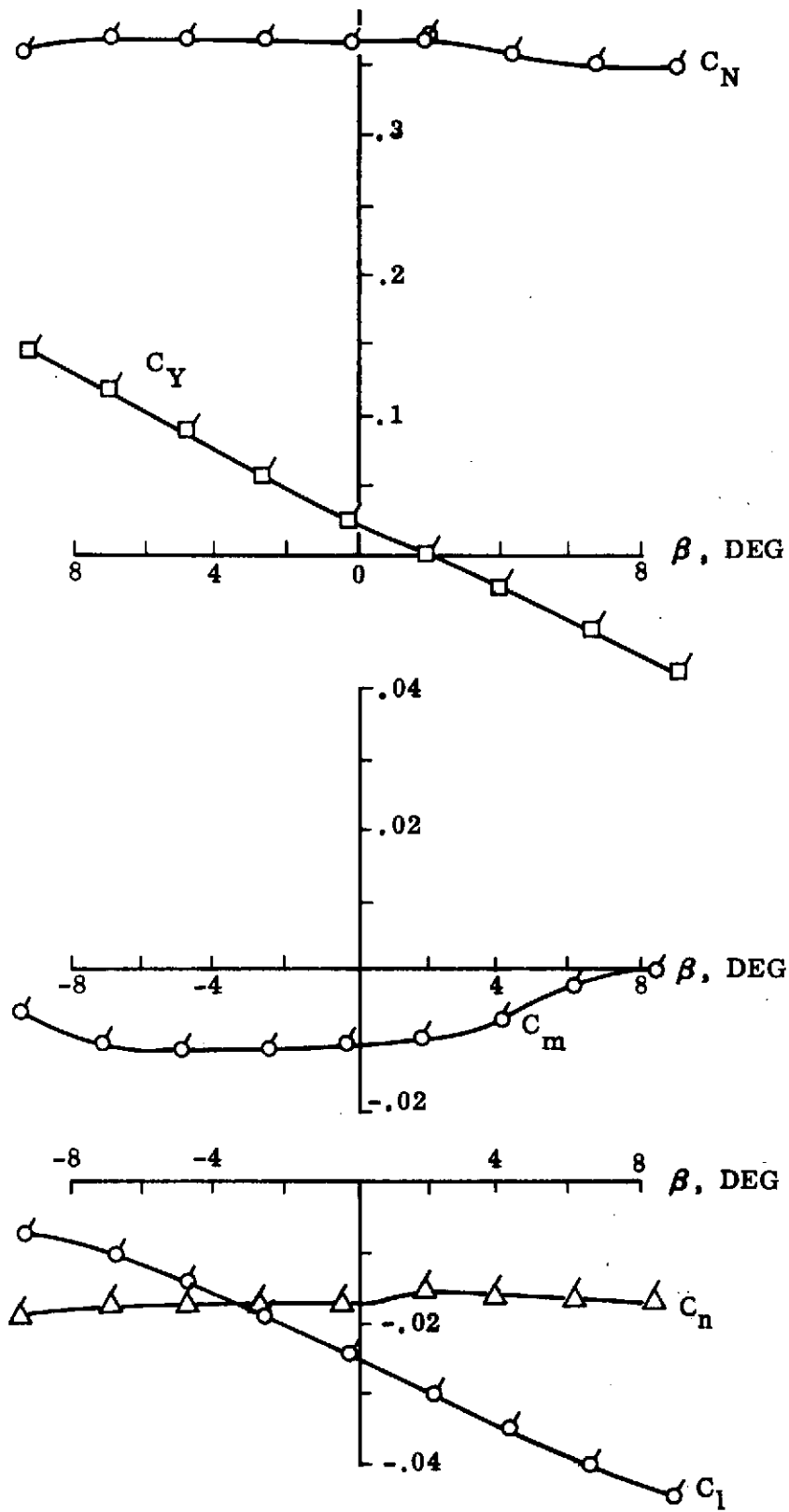


Figure 14. 040A Orbiter Yaw Stability,
 $M = 1.46$, $\alpha = 11.4^\circ$, $\delta_L = -40^\circ$, $\delta_R = 0$

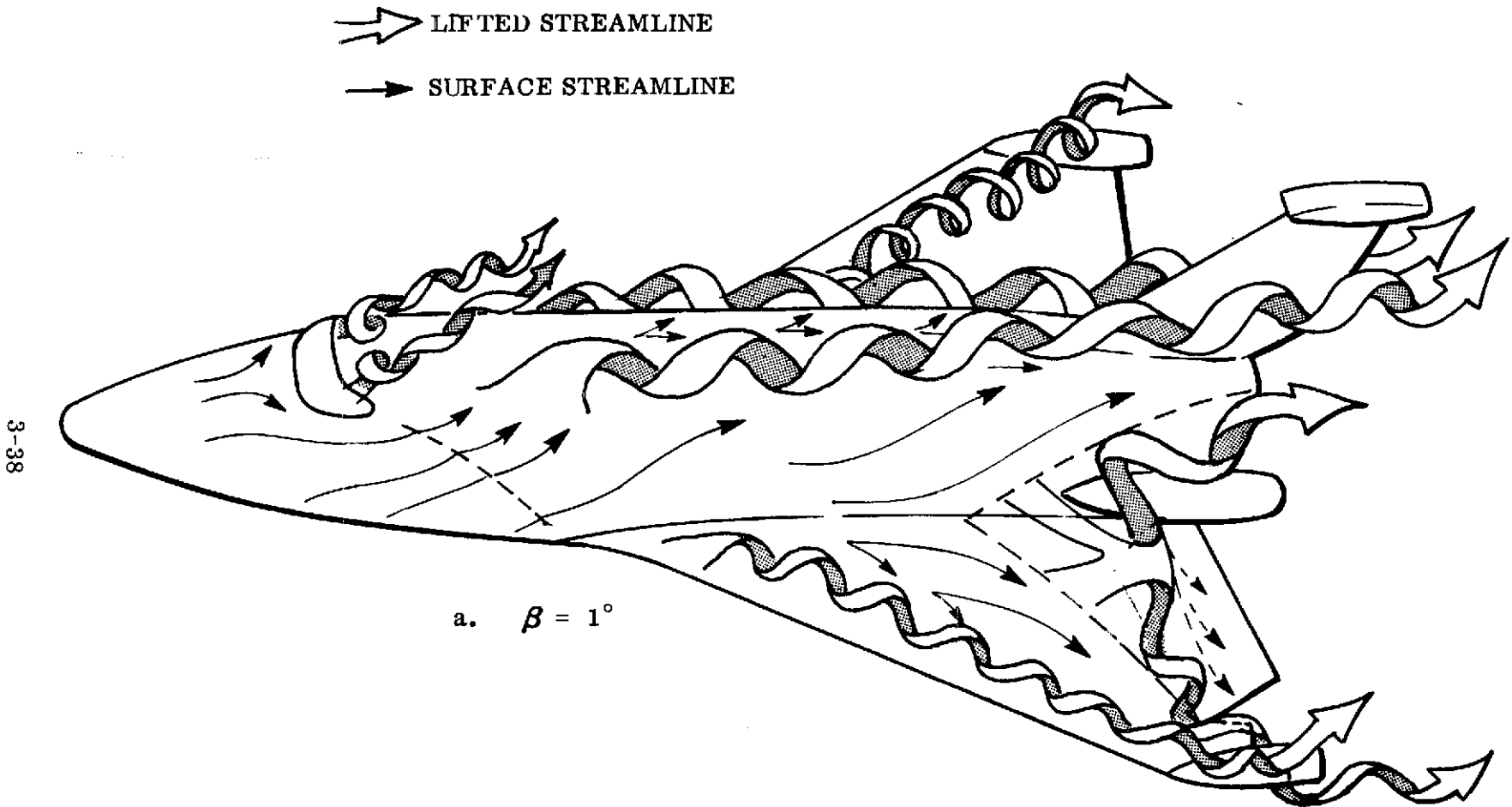


Figure 15. 040A Orbiter Flow Field due to Yaw at $M = 0.9$, $\alpha = 10^\circ$, $\delta_L = -40^\circ$, $\delta_R = 0$
(Sheet 1 of 2)

⇨ LIFTED STREAMLINE
→ SURFACE STREAMLINE

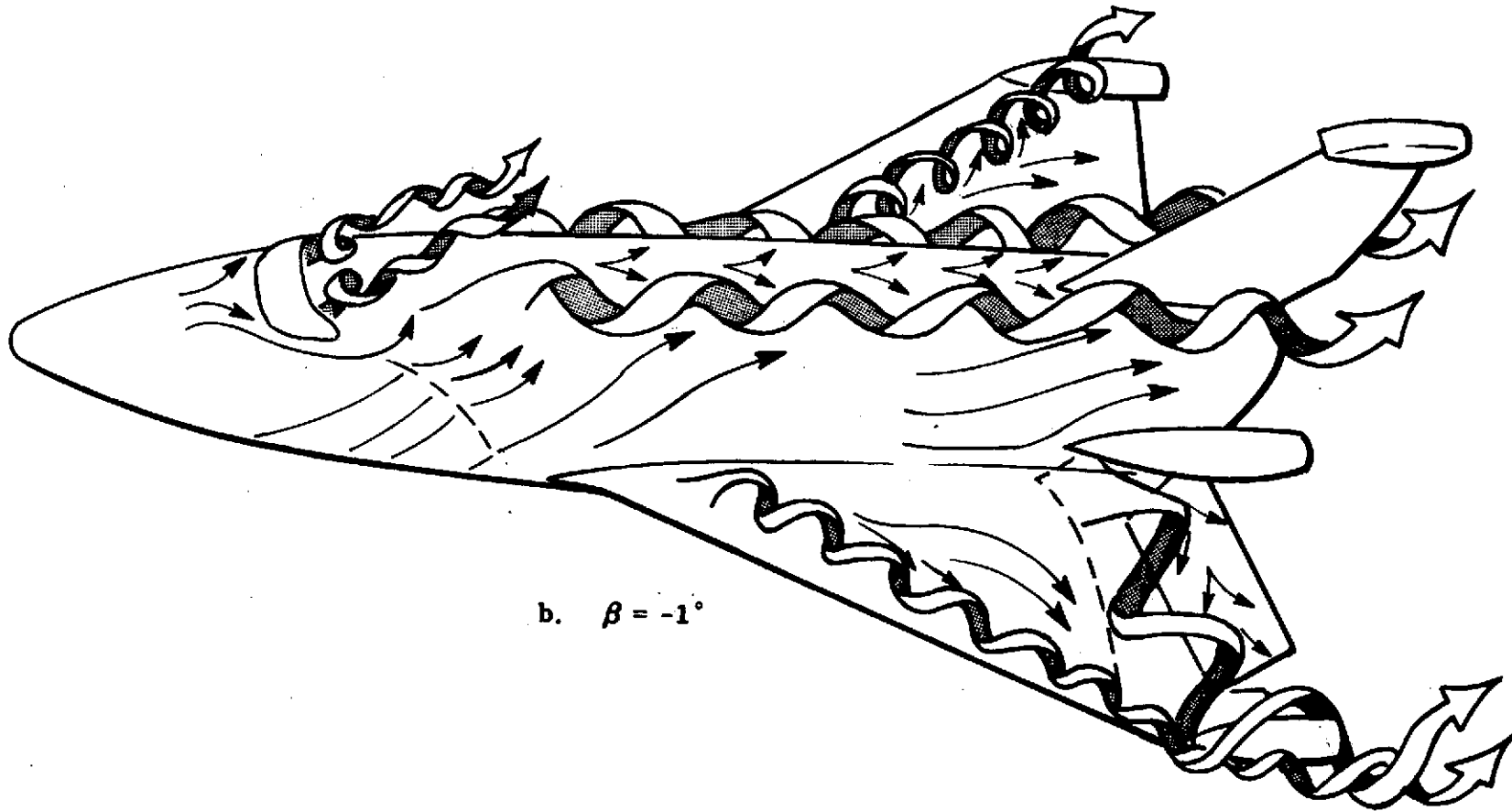
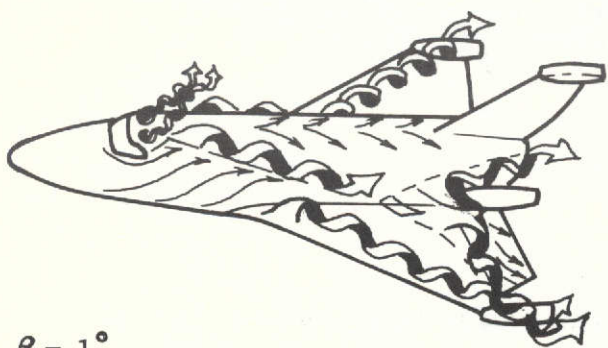
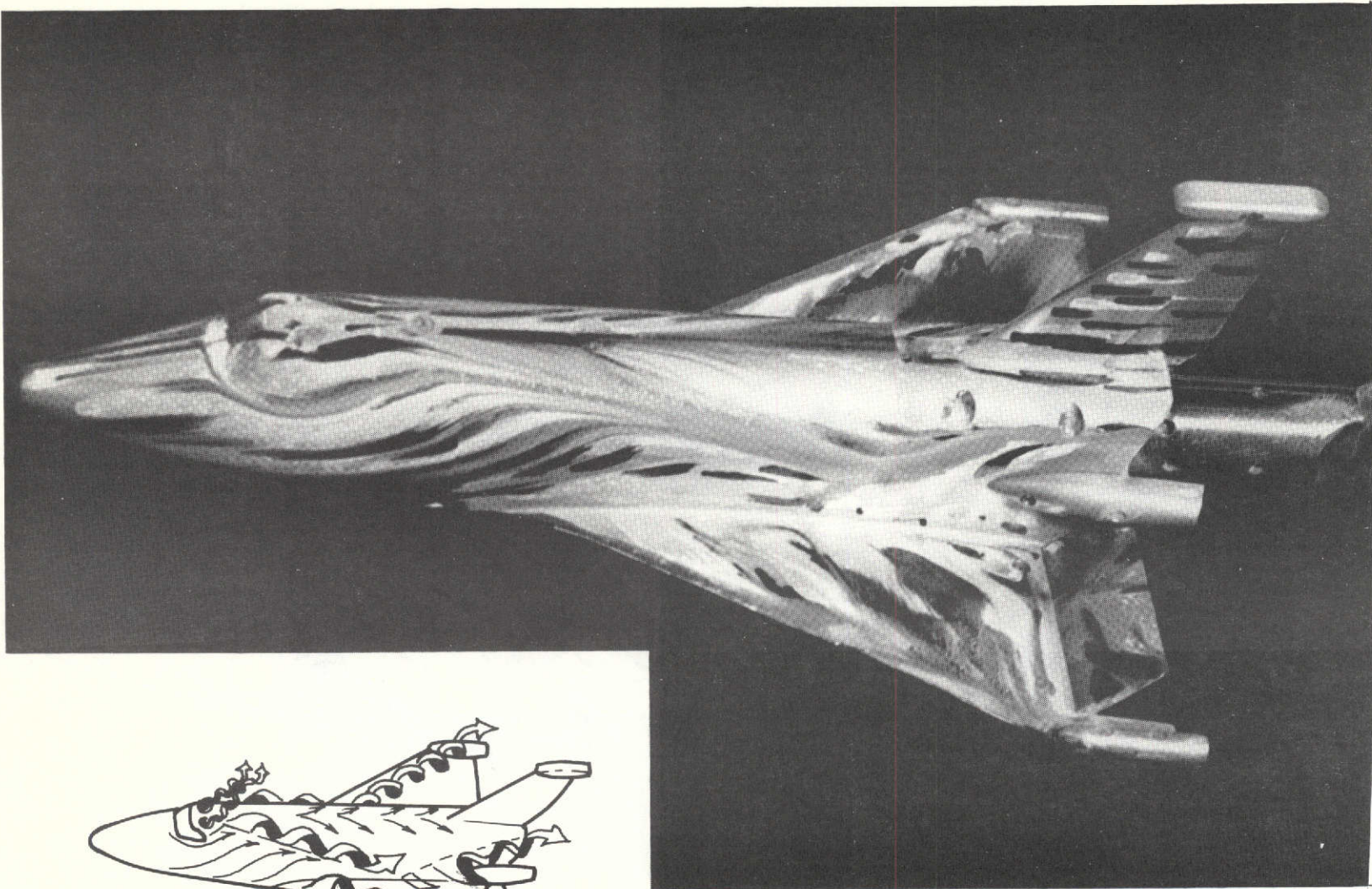




Figure 15. 040A Orbiter Flow Field due to Yaw at $M = 0.9$, $\alpha = 10^\circ$, $\delta_L = -40^\circ$, $\delta_R = 0$
(Sheet 2 of 2)

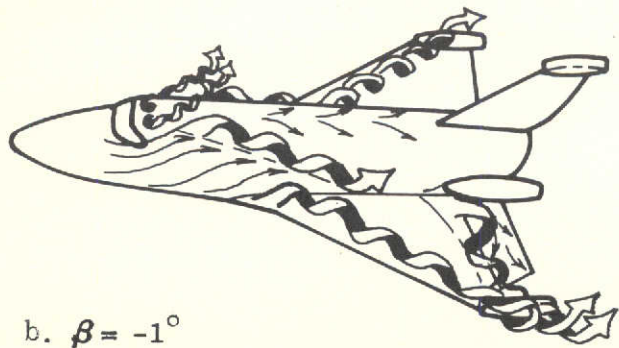
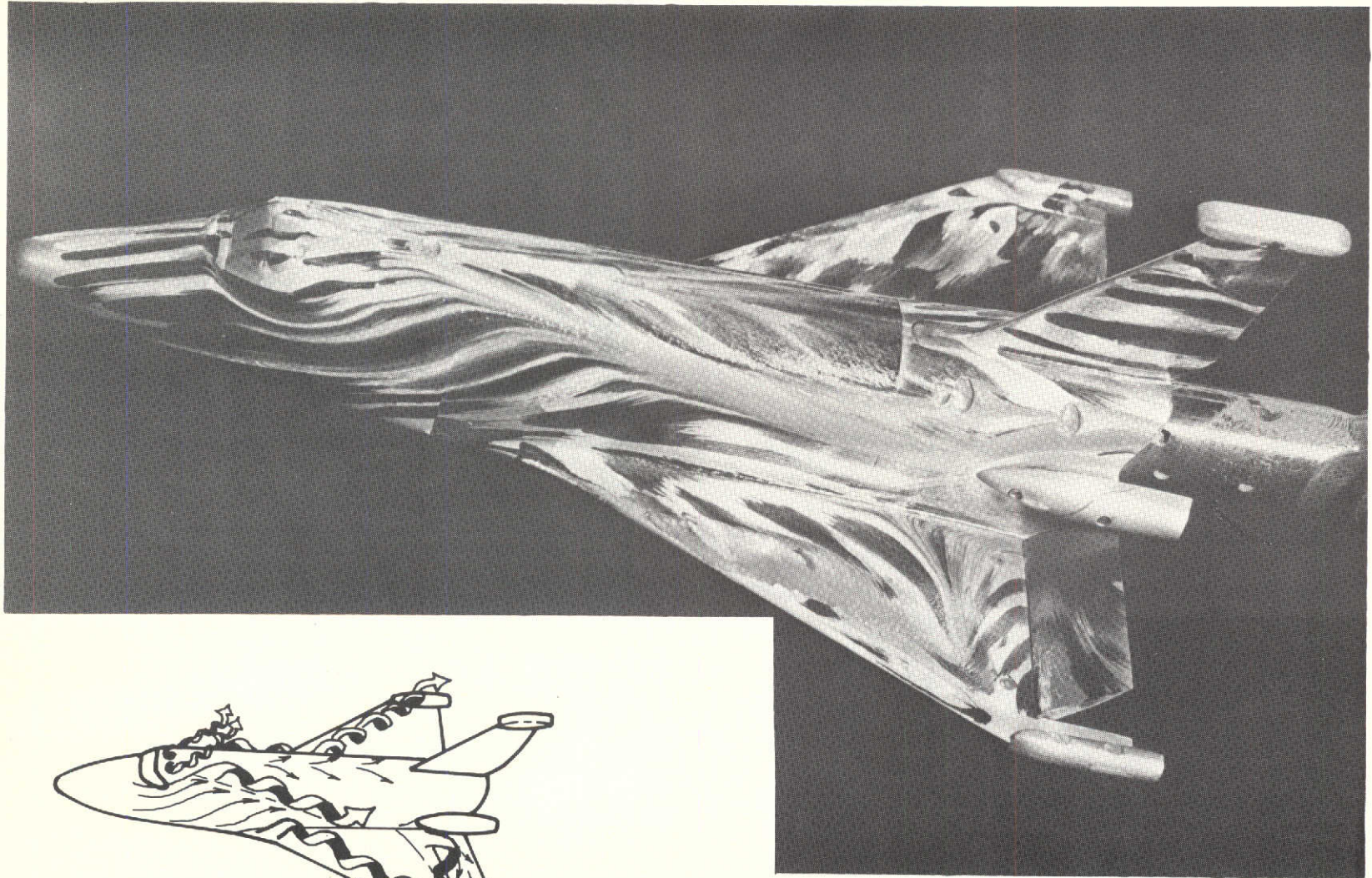


 LIFTED STREAMLINE
 SURFACE STREAMLINE

a. $\beta = 1^\circ$

Figure 16. 040A Orbiter Surface Flow Patterns Due to Yaw at $M = 1.46$,
 $\alpha = 11^\circ$, $\delta_L = -40^\circ$, $\delta_R = 0$ (Sheet 1 of 2)

3-41



b. $\beta = -1^\circ$

⇨ LIFTED STREAMLINE
⇨ SURFACE STREAMLINE

Figure 16. 040A Orbiter Surface Flow Patterns Due to Yaw at $M = 1.46$,
 $\alpha = 11^\circ$, $\delta_L = -40^\circ$, $\delta_R = 0$ (Sheet 2 of 2)

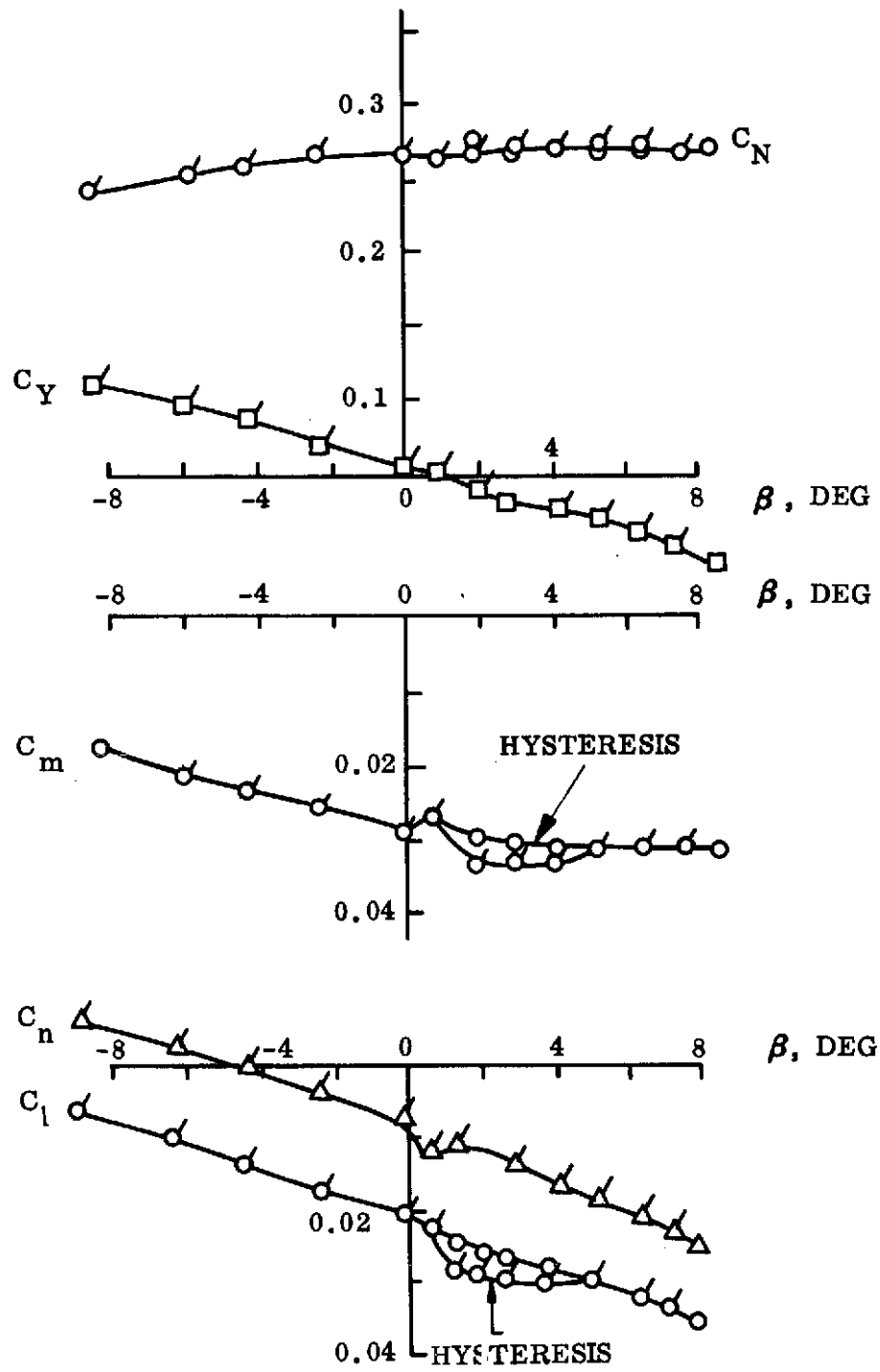


Figure 17. 040A Orbiter Yaw Stability,
 $M = 1.46$, $\alpha = 22.4^\circ$, $\delta_L = -40^\circ$, $\delta_R = 0$

3-43

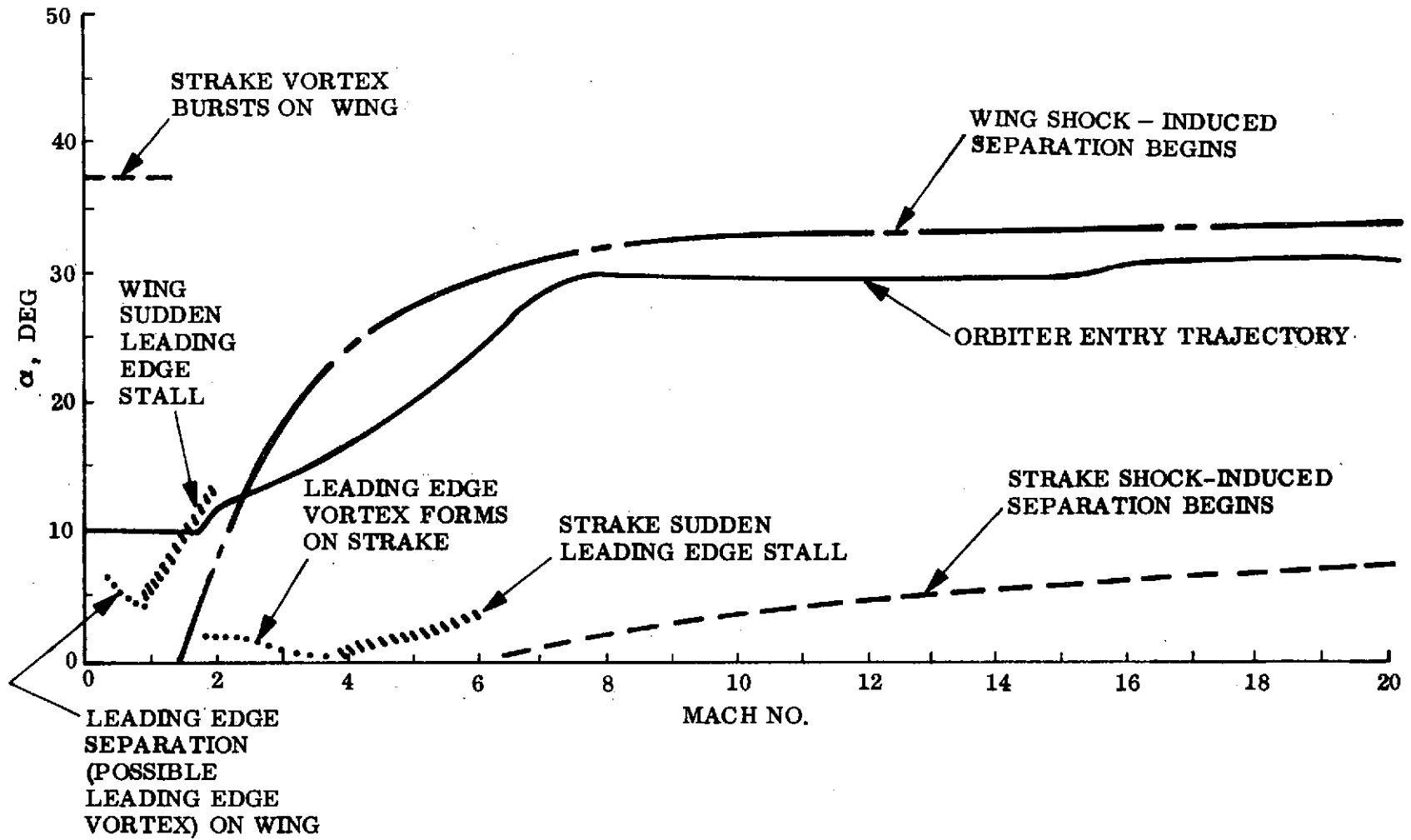


Figure 18. Estimated Unsteady Flow Boundaries for Current Orbiter

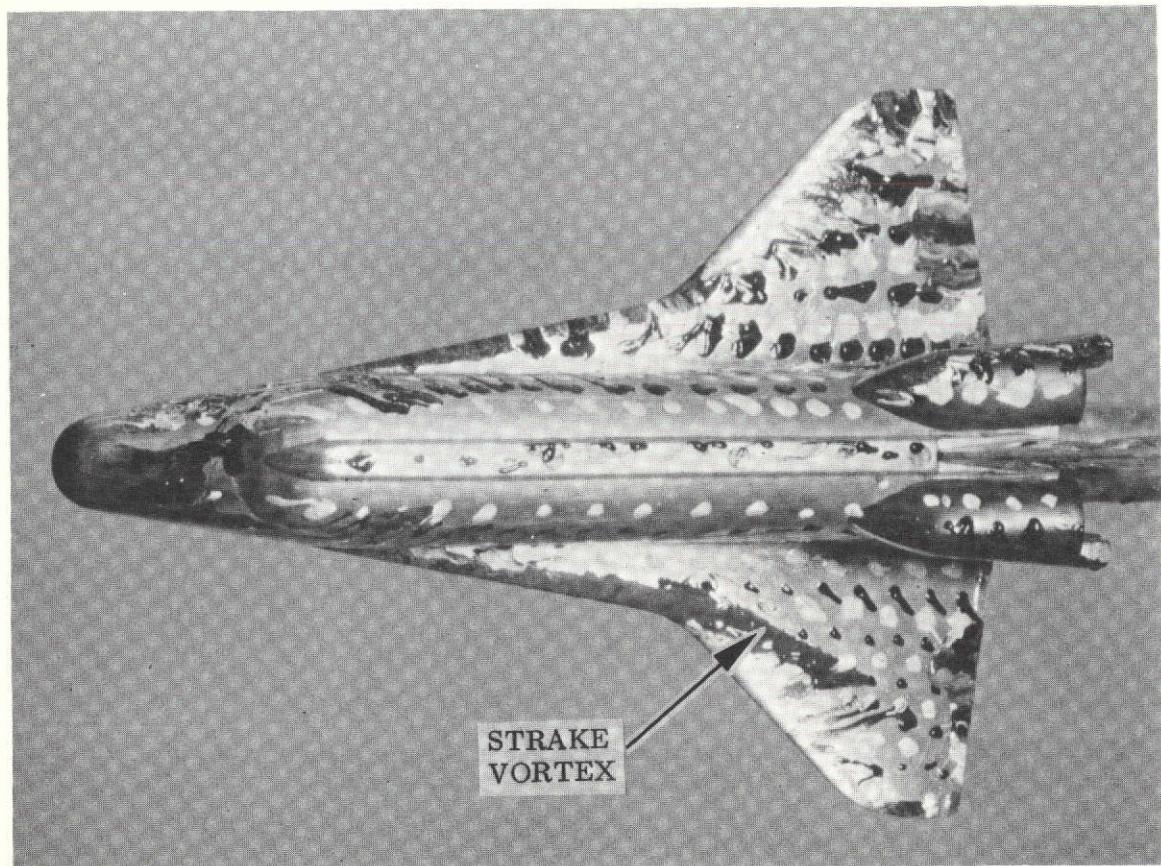


Figure 19. Evidence of Strake Vortex on Current Orbiter,
 $M = 4.96$, $\alpha = 20^\circ$, $\beta = 0$

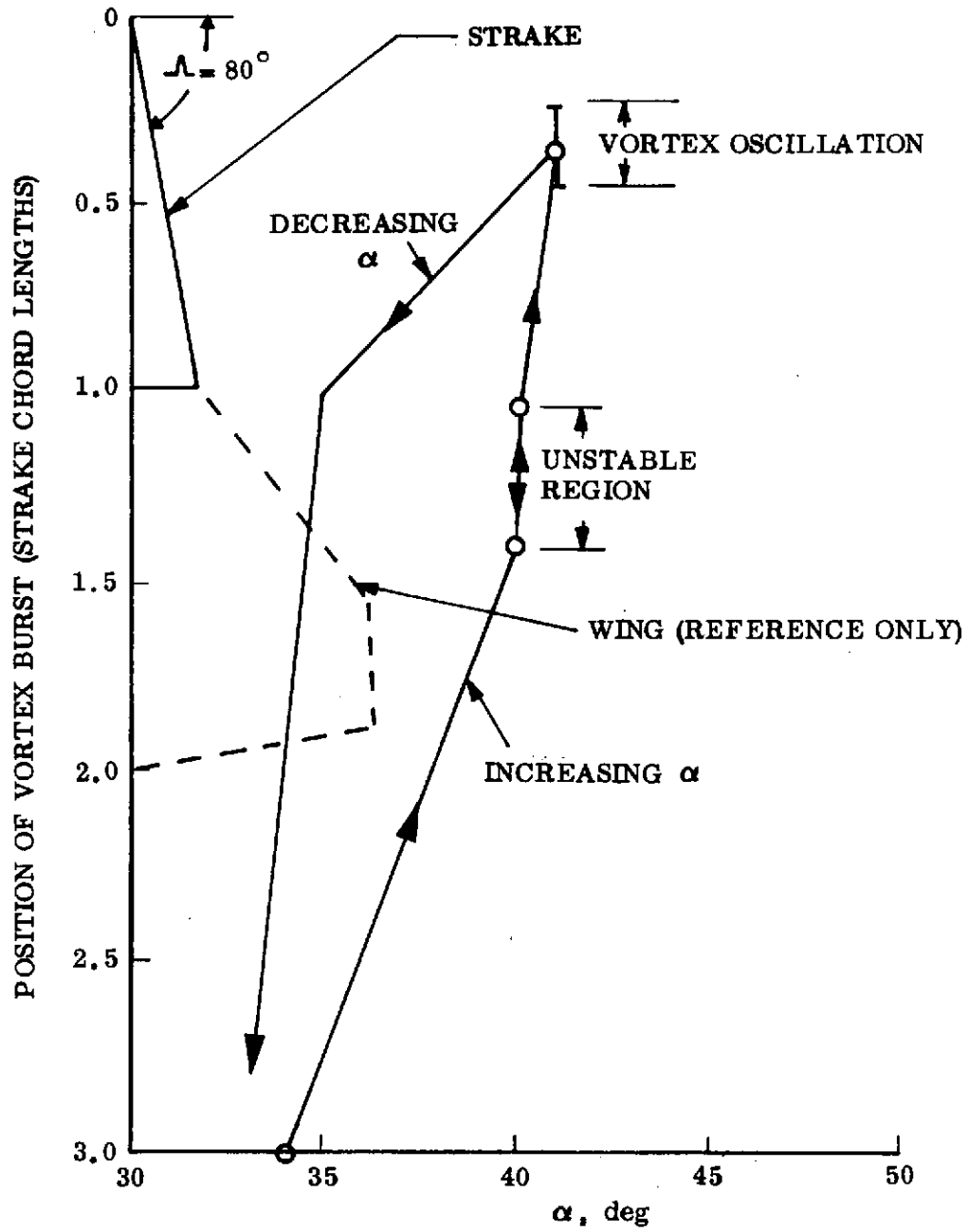


Figure 20. Vortex Burst Location and Hysteresis for Strake Alone at Subsonic Speeds

Section 4

CONCLUSIONS

A wind tunnel test has been conducted to explore the unsteady aerodynamics of the 040A space shuttle orbiter. The results have verified that many of the unsteady flow boundaries can be predicted reasonably well. The test also revealed a previously unknown region of discontinuous yaw stability characteristics. Even though the orbiter configuration has changed, these results give insight into the causes of the various flow separation effects that can occur also on the new orbiter.

The unsteady aerodynamic effects that are likely to dominate the dynamics of the current orbiter have been identified. They are:

1. Shock-induced separation
2. Sudden leading edge stall
3. Burst of the strake vortex
4. Discontinuous yaw characteristics.

These are essentially the same problems faced by earlier designs. However, the point where they occur in the entry trajectory is sensitive to configuration details. The results from the present test, combined with the experience gained from previous studies, permit predictions to be made of the regions of shock-induced separation, sudden stall, and vortex burst for the nominal entry trajectory with $\beta = 0$ and $\delta = 0$. A wind tunnel test is recommended that will allow better definition of these boundaries, especially in regard to the effects of reasonable variations of attitude (pitch, yaw, roll) and control deflection about the nominal values. The test should also provide sufficient quantitative data to make a preliminary assessment of the seriousness of the various unsteady flow effects. Any wind tunnel test of the shuttle orbiter will present simulation difficulties because Reynolds number, roughness, and possibly heat transfer have significant effects on the occurrence and extent of the separated flow.

Section 5
RECOMMENDATIONS FOR FUTURE STUDY

It is shown in the foregoing that the current orbiter is likely to encounter the following unsteady flow effects:

1. Shock-induced separation on the wing
2. Sudden leading edge stall
3. Elevon-induced burst of the strake vortex
4. Possible elevon-induced discontinuous yaw derivatives.

If any of these effects are judged to be a problem relative to flight dynamics, various courses of action can be taken. The trajectory can be altered to avoid the critical unsteady flow region; the configuration can be altered to eliminate the problem; or the instability may be controlled via stability augmentation. Before a course of action can be chosen, one needs to know the causes of the unsteady flow effects and the extent of the unsteady flow region relative to the entry trajectory for practical variations of α , β , and δ . Also desirable would be a quantitative measure of the effects on both static and dynamic stability derivatives. Outlined below is a static wind tunnel test program to supply these needed data. The static results can be used in a single-degree-of-freedom dynamic stability analysis (e.g., Ref. 18) to provide a preliminary assessment of the seriousness of the problem. At some later date, special dynamic tests or a more involved analysis will probably be appropriate.

The experimental approach should be similar to but more complete than that reported herein for the 040A orbiter. That is, the initial investigation of the unsteady flow region will involve deflection of only one elevon. This allows roll, yaw, and side force data to be used more effectively in gaining a thorough understanding of the phenomena involved. Good quality flow visualization results are vital to an understanding of these complicated, interactive unsteady flows. Both oilflow photographs

and shadowgraphs should be obtained for all critical flow conditions. Data should also be obtained for realistic deflections of both elevons for certain critical cases. Generally, it may be possible to compute the effects of combined deflection from data obtained with only one elevon deflected because there is usually very little "cross talk" or coupling between the wing flows. However, when the elevon-induced separation induces body crossflow and alters the leeside vortex trajectories, as frequently happened on the 040A orbiter, strong coupling effects are to be expected.

These results should reveal the important unsteady flow regions. However, it may be necessary to explore other flight conditions (particularly other Mach numbers) to adequately map the unsteady flow regions. Table I summarizes some typical test conditions. Item 1 concerns strake vortex burst. At hypersonic speeds, the orbiter may encounter burst of the strake vortex even at $\delta = 0$ because of the high angle of attack or upstream effects of the near wake. The wing wake recompression shock has been observed to induce separation of the leeside of a wing at hypersonic speed (Ref. 19). Thus, even when $\delta = 0$, a shock-induced separation will occur on the wing which can affect the vehicle dynamics directly. Items 2 and 3 are straightforward investigations of shock-induced separation and sudden stall respectively. Because discontinuous yaw characteristics could occur throughout the entry trajectory, item 4 covers the entire Mach number range in the search for these effects. That elevon-induced vortex burst could also occur throughout entry is reflected by the item 5 test conditions.

It is possible that shock-induced separation can be converted to sudden stall due to elevon back-pressure effects. Furthermore, the change in stall pattern may persist even after the elevon deflection is reduced below the critical value (Ref. 1). Therefore, it is highly desirable to be able to remotely deflect the elevons to investigate this possible hysteresis. Elevon-induced burst of the strake vortex is likely to exhibit similar hysteresis effects, raising further demands for remote elevon deflection capability.

An issue of major concern for the proposed test program is the poor Reynolds number scaling one is forced to accept when trying to simulate the flight conditions

Table I Summary of Test Conditions

<u>Item</u>	<u>Unsteady Flow Effect</u>	<u>Test Mach</u>	<u>α range</u>	<u>β range</u>	<u>δ range</u>
1	Strake vortex burst	5.0 and 8.0	15° → 35°	0	0
2	Shock-induced separation	1.5 → 3.0	0 → 30°	0	0 → -40°
3	Sudden leading edge stall	0.9 → 2.0	0 → 20°	0	0 → -40°
4	Discontinuous yaw characteristics	8.0	30°	±10°	0 → -40°
		5.0	20°	±10°	0 → -40°
		3.0	15°	±10°	0 → -40°
		2.0	12°	±10°	0 → -40°
		1.5	10°	±10°	0 → -40°
		0.9	10°	±10°	0 → -40°
		0.6	10°	±10°	0 → -40°
		0.3	10°	±10°	0 → -40°
		5	Elevon-induced burst of strake vortex	5.0 and 8.0	15° → 35°
1.5 → 3.0	0° → 30°			±10°	0 → -40°
0.3 → 2.0	0° → 20°			±10°	0 → -40°

of a vehicle as large as the shuttle. This is a particularly sensitive question where flow separation is concerned, because the separation-induced forces (the very forces which one wishes to measure) are known to be very sensitive to Reynolds number effects. Particular care must therefore be taken in the selection and placement of boundary layer trips or distributed roughness. The simulation of the full-scale location of a terminal normal shock (and the associated separated region) was achieved in the wind tunnel by positioning the boundary layer trip so that the boundary layer characteristics at the trailing edge were scaled (Ref. 20). A similar technique could be used for the present test. Since a significant separation occurs on the fuselage sides, it will be necessary to scale the boundary layer at the fuselage base as well as the wing trailing edge. Of special concern is the scaling of the aerodynamics of the free fuselage vortices. It has been found, for instance, that the strong vortex-induced loads that led to spin divergence in the wind tunnel were not realized in flight (Ref. 21). The reason was the poor Reynolds number simulation in the wind tunnel. The boundary layer over the slender nose was laminar in the wind tunnel, with a subcritical separation location in the crossflow plane; whereas the boundary layer was turbulent in flight and the separation was supercritical, which resulted in much weaker asymmetric vortex shedding (Ref. 22). Other examples of similar scaling difficulties appear in Ref. 1. The present orbiter configuration will not experience the same effects of free-body vortices owing to the blunt nose, different α -M history, and the noncircular forebody fuselage cross section. However, the 040A data indicate that body or fuselage vortices can play a significant part in the orbiter aerodynamics, and proper scaling must therefore be ensured.

The occurrence of boundary layer transition and separation on the wing will be affected by the orbiter dynamic motion. Refs. 23 and 24 show that the pitch rate affects flow separation and transition on a wing. This cannot be simulated in a static test and must eventually be investigated analytically or in special dynamic tests, or both.

Recent experimental results (Ref. 25) imply that it may be necessary to simulate the hot orbiter structure in order to obtain correct scaling of the separated flow region. The orbiter will be hot after entry, and the resulting heat transfer to the boundary layer promotes separation. Thus, it is desirable to simulate the wall to free stream temperature ratio, if possible. This might require heating the model by some means.

Section 6
REFERENCES

1. Reding, J. P. and Ericsson, L. E., "Review of Delta Wing Space Shuttle Vehicle Dynamics," Report LMSC-D243938, October 1971, Lockheed Missiles & Space Company, Sunnyvale, California.
2. Simon, E., "Calibration Tests of the MSFC 14x14 inch Trisonic Wind Tunnel," NASA TMX-53113, August 2, 1964.
3. Lindsey, W. F. and Landrum, E. J., "Compilation of Information on the Transonic Attachment of Flows at the Leading Edges of Airfoils," NACA TN 4204, February 1958.
4. Click, P. L., Michner, D. J., and Surver, D. A., "Aerodynamic Stability and Control Characteristics of the NASA/MSC .006 scale 040-A Delta Wing Orbiter," NASA DMS-DR-1186, Nov. 1971.
5. Hummel, D., "Untersuchungen über das Aufplatzen der Wirbel an schlanken Delta-flügeln," Zeitschrift für Flugwissenschaften 13, 1965, pp. 158-168.
6. Ericsson, L. E., "Aeroelastic Instability Caused by Slender Payloads," Journal of Spacecraft and Rockets, Vol. 4, No. 1, Jan. 1967, pp. 65-73.
7. Lawson, M. V., "Some Experiments with Vortex Breakdown," Journal of the Royal Aeronautical Society, Vol. 68, May 1964, pp. 343-346.
8. Cross, E. J., "Analytical Investigation of the Expansion Flow Field over a Delta Wing at Hypersonic Speeds," ARL 68-0027, Feb. 1968.
9. Seegmiller, H. L., "Surface Flow Visualization Investigation of a High Cross Range Shuttle Configuration at a Mach Number of 7.4 and Several Reynolds Numbers," NASA SSPD-8, June 2, 1970.
10. Kuehn, D. M., "Experimental Investigation of the Pressure Rise Required for the Incipient Separation of Turbulent Boundary Layers in Two-Dimensional Supersonic Flow," NASA Memo 1-21-59A, Feb. 1959.

11. Reding, J. P. and Ericsson, L. E., "Effects of Delta Wing Separation on Shuttle Dynamics," Journal of Spacecraft and Rockets, Vol. 10, No. 7, July 1973, pp 421-428.
12. Hamilton, E. J. and Ryals, W. G., "Review of 1/10 Scale Shuttle Air Drop Test Results," MSC Internal Document 5-2950-1-HOU-126, June 1970, NASA.
13. Graham, D., "The Low-Speed Lift and Drag Characteristics of a Series of Airplane Models Having Triangular or Modified Triangular Wings," NACA RM A53D14, June 15, 1953.
14. Wentz, W. H., Jr. and Kohlman, D. L., "Vortex Breakdown on Sharp-Edged Wings," AIAA Paper No. 69-778, July 1969.
15. Mullons, E. and Linsley, C. E., "Buffet Dynamic Loads during Transonic Maneuvers," AFFDL-TR-72-46, Sept. 1972, Air Force Flight Dynamic Laboratory, Wright-Patterson Air Force Base, Ohio.
16. Wentz, W. H., Jr. and McMahon, M. C., "Further Experimental Investigations of Delta and Double-Delta Wing Flow Fields at Low Speeds," NASA CR-714, February 1967.
17. Ray, E. J., McKinney, L. W., and Carmichael, J. G., "Maneuver and Buffet Characteristics of Fighter Aircraft," Paper 24, AGARD Specialists' Meeting on Fluid Dynamics of Aircraft Stalling, Lisbon, Portugal, April 26-28, 1972.
18. Ericsson, L. E. and Reding, J. P., "Analysis of Flow Separation Effects on the Dynamics of a Large Space Booster," Journal of Spacecraft and Rockets, Vol. 2 No. 4, July-August 1965, pp. 481-490.
19. Hulcher, G. D. and Behrens, W., "Viscous Hypersonic Flow over a Flat Plate at Angle of Attack with Leaside Boundary Layer Separation," Proceedings of the 1972 Heat Transfer and Fluid Mechanics Institute, Northridge, California, June 1972.
20. Blackwell, J. A., Jr., "Preliminary Study of Effects of Reynolds Number and Boundary-Layer Transition Location on Shock-Induced Separation," NASA TN D-5003, January 1969.

21. Anderson, C. A., "Stall/Post-Stall Characteristics of the F-111 Aircraft," Paper No. 18, AGARD Specialists Meeting on Fluid Dynamics of Aircraft Stalling, Lisbon, Portugal, April 26-28, 1972.
22. Ericsson, L. E., "Report on Visit to the AGARD Specialists' Meeting on the Fluid Dynamics of Aircraft Stalling," Lisbon, Portugal, April 26-28, 1972, LMSC-TIC-2061, Sept. 1972.
23. Ericsson, L. E., "Effects of Boundary Layer Transition on Vehicle Dynamics," Journal of Spacecraft and Rockets, Vol. 6, No. 12, Dec. 1969, pp. 1404-1409.
24. Ericsson, L. E., and Reding, J. P., "Unsteady Airfoil Stall and Stall Flutter," NASA CR-111906, June 1972; also Report No. A6J-71-1, Lockheed Missiles & Space Company, Sunnyvale, California.
25. Macha, J. M., Norton, D. J., and Young, J. C., "Surface Temperature Effects on Subsonic Stall," AIAA Paper No. 72-960, September 1972.

Appendix A
NOMENCLATURE

A	axial force: coefficient $C_A = A/(\rho_\infty U_\infty^2/2)S$
a	speed of sound
AR	aspect ratio, $AR = b^2/S$
b	wing span
c	reference length, $c = \Delta$ wing mean aerodynamic chord
ℓ	rolling moment: coefficient $C_\ell = \ell/(\rho_\infty U_\infty^2/2)Sb$
M	Mach number, $M = a/U$
M_p	pitching moment: coefficient $C_m = M_p/(\rho_\infty U_\infty^2/2)Sc$
N	normal force: coefficient $C_N = N/(\rho_\infty U_\infty^2/2)S$
n	yawing moment: coefficient $C_n = n/(\rho_\infty U_\infty^2/2)Sb$
S	reference area
U	free stream velocity
Y	side force: coefficient $C_Y = Y/(\rho_\infty U_\infty^2/2)S$
α	angle of attack
β	sideslip angle
δ	control deflection (positive trailing edge down)
Λ	sweep angle of leading edge
ρ	air density
ϕ	roll angle
ψ	yaw angle

Subscripts

CG	center of gravity
L	left
R	right
∞	free stream conditions
α	$\partial/\partial\alpha$
β	$\partial/\partial\beta$
δ	$\partial/\partial\delta$